THE EFFECT OF PRINT STYLE ON MECHANICAL AND MICROSTRUCTURAL PROPERTIES OF STRUCTURAL CERAMICS FABRICATED VIA THREE-DIMENSIONAL PRINTING

by

Bugra Giritlioglu

B.S. Materials Science and Engineering, 1993
Cornell University, Ithaca, NY

Submitted to the
Department of Materials Science and Engineering
in Partial Fulfillment of the Requirements
for the Degree of

MASTER OF SCIENCE

in Materials Science and Engineering
at the

Massachusetts Institute of Technology

February, 1996

Signature of Author_____
Department of Materials Science and Engineering
January 19, 1996

Certified by_____
Michael J. Cima
Norton Associate Professor of Ceramics
Thesis Supervisor

Accepted by_____
Michael F. Rubner
TDK Professor of Materials Science and Engineering
Chair, Departmental Committee on Graduate Students

THE EFFECT OF PRINT STYLE ON MECHANICAL AND MICROSTRUCTURAL PROPERTIES OF STRUCTURAL CERAMICS FABRICATED VIA THREE-DIMENSIONAL PRINTING

by

Bugra Giritlioglu

Submitted to the
Department of Materials Science and Engineering
on January 19, 1996 in partial fulfillment of the requirements
for the degree of Master of Science in Materials Science and Engineering

ABSTRACT

Three-dimensional printing (3DP) is a solid freeform fabrication technique that utilizes ink jet type print heads to place binder droplets in a computer-specified pattern onto layers of powdered materials, gluing the powder bed on a point-by-point basis. The mechanical and microstructural properties of green and fired parts depends strongly on the specific manner in which droplets are deposited onto the powder bed, i.e. the print style. In particular, line spacing, layer height, droplet placement, line arrangement are among the important parameters.

The effects of print style was investigated by printing 3 sets of bars out of spray dried alumina using 3 print styles, viz. the linear raster, staggered, and checker styles. Each set consisted of 3 types of long rectangular bars oriented along the 3 orthogonal axes of the 3D printer. Four-point bend testing was performed on as-printed bars as well as Cold Isostatically Pressed (CIP) & fired bars. The dependence of Modulus of Rupture (MOR) on direction and print style was determined. Shrinkage due to CIP along the 3 axes was quantified. SEM and optical microscopy was used to characterize microstructure of green and fired parts. Current CIP technique was modified to allow CIP of complex shapes with hollow interiors. A prechamber part was fabricated using this new technique.

Green parts were strongest along the fast axis, weakest along the z axis, with an MOR ratio of ~3. WIP & firing virtually eliminated the defect/strength anisotropy observed in as-printed green parts. The staggered style reduced the number and size of 3DP-induced intergranular porosity by preventing line merging. The staggered bars yielded the highest fired alumina strengths (~400 MPa). Proportional deflection improved green strength along the slow axis. The average strength for silicon nitride bars was ~570 MPa.

Thesis Supervisor: Dr. Michael J. Cima
Title: Norton Professor of Ceramics

ANAGRAMATICALLY YOURS,

I am really sorry about the small font but I had to do it to correct a big big page number error somewhere else. This might save my life...

Can you figure out who the following are?? If not, see solutions at the end

To thank Professor "I am chemical," a.k.a "I am a chic male" I would like very much (1) Over the past two years, for all his guidance, and for beyond graduation agreeing to hire me , thereby, for the time being, from the horrors of the Turkish military saving me, I owe him a lot! Out of the way is this degree thing now. Like, forward to a fruitful and less stressful collaboration I'm looking, I mean, like, some fun time together. (English or no English, is that the question??!)

I would also like to thank Professor "humane scales," a.k.a. "has mean clues," or "such mean sale" (2) for all his support, especially for helping me get on the alphamachine queue just at the right time... If it weren't for him, I could still be doing experiments now!

"Jist a Arab hunk!" a.k.a. "It's Arab junk!" (3) The latter anagram used to come up quite frequently in regards to the mess that a certain friend of ours used to habitually leave behind! Watch out for (3) he's gotta be the fastest paper towel drawer in all of the East! Nobody has put them to as many uses as he either-- data collection, warpage demos. He always has the "enthu" to clarify a point or two right on the spot (of course, he finds the marker/paper towel combination the most convenient for that purpose also! "let's just...why don't we jot down the main issues..." will say the master. And of course he has always "done those experiments," and "has those results..." "just has to dig them out") He will make you laugh in the direst of situations. It was a lot of fun working and joking around with you. Thanks for making the whole CPRL experience an enjoyable one. Looking forward to more bitching sessions together in the coming months! (he got away with botheration but I don't know about "viction"... I'd say he's really pushing it!)

"Okay Joe Doe!" (4) is the second person who has helped me a lot over the past two years, especially when I first arrived here. Like his anagram suggests, he says "OK" a lot when he's explaining stuff! He used to diligently and tirelessly direct me towards the cage every time I looked for something until I finally realized that the "cage" contained just about anything you needed (except maybe love). At times, I must admit, your overmeticulousness gets to me, but I greatly admire your persistence and determination in life, my friend. I know that you *will* go straight to heaven some day-- but don't forget your promise to take the protomachine there with you!

I also thank my officemate "never irk less" a.k.a. "reverse links" (5) in joining hands with "No! Bring seven Ellen!" (6) in constantly teasing and annoying me over the past two years. You actually never got me. I'm just really good at pretending that I'm scared. You will have my "favorite American" as a wife soon. And I must admit you too look really cute together! I wish you the best in the near and far future.

The only redeeming feature of "No! Bring seven Ellen!" (6) is his twin sons. They are absolutely adorable and it's a wonder (and perhaps a pity) that they have any genetic ties to (6). Watch out for this guy-- he will start pulling your leg before he's even met you! (ask Karina if

you don't believe me!) He's kinda arrogant and condescending, and he also will get ticked off by just about anything. Oh, and he also has this really straaaaange accent. Otherwise, he's an alright guy. I owe him lots of thanks for all the computer help. Take care, and keep on wearing blue. Blue's you!

"shan't join in" a.k.a "oh! isn't jan in??" (7) is just another Italian stallion at CPRL (the last to join the club) and he's in many ways the last straw that broke the camel's back but we won't get into that!

"Rumanian Model" "An immoral nude!" "Dream on Alumni!" (8) This guy is just rrrrrrreally rrrrrrreally notorrrrrrrrious forrrrrr rrrrrrrrrrrolling his rrrrrrrrs and forrrrrrgetting to clean up afterrrrrrrr himself. But he's alrrrrrrright otherrrrrrwise. Thanks for all the help. Hope to see you again some day.

And here is the absolute winner as far as anagrams... This person's name was made for anagrammatization. (you rule, man!!) Without further delay, here is:

"esoteric man" "MA secretion" "nice maestro" "Erection Sam!" "come nastier"
"romance ties" "men's erotica" "I ascent Rome" "a cosine term" "erotic amens"
"no secret aim" "crime: ate son!" "enter Ms. Ciao" "A Rome incest" "A Rome insect"....(9)
Not too bad, eh??

Solutions to the anagrams:
(1) Michael Cima, (2) Emanuel Sachs, (3) Satbir Khanuja, (4) Jaedeok Yoo, (5) Kevin Ressler, (6) Neville Sonnenberg, (7) John Santini, the studio for hair. (8) Daniel Nammour, (9) Cesare Monti.

Sorry, I don't have anagrams for the rest of you guys :-(

John Jack Smith, thanks for enlightening me on so many different topics over the past two years. Only you would have a story about a food truck driver momentarily resting a huge chunk of raw meat of unknown origin directly on ancient driver's seat (edited by Jack himself!)

Karina Rigby, you will always be a really nice and sensitive girl no matter how hard you try to be the tough woman engineer :-) And I will always cherish the memory of our (leider einmalige) close friendship... Ausgezeichnet! Party weiter! (Wayne's Welt)

Jason Grau, thanks for listening to my babbling on various research dilemmas and giving me advice along the way and also for all the help with the porosimetry. I'm glad your stomach is OK; don't let CPRL give you a ulcer, I'm looking forward to working with you for a while longer.

John Centorino, thanks for all the help and sorry for all those times that I forgot to log in and the times that I almost gave you a heart attack by coming really close to blowing up the Centorr! Take care and I will see you in a month.

Lenny Regione, I owe you lots of thanks for going out of your way to explain stuff in great detail (including English clarifications), always providing tips above and beyond what a standard training session might be expected to include. I think we all owe you for being such a

meticulous and methodical guy. Thanks for all the help with spray-drying, sieving, and so on, but above all thanks for being around, esp. when I needed to talk to somebody at strange hours in the lab.

Barbara Layne, thanks for putting up with my childish ways, and my rubber bands! I think I finally got that rubber band throwing technique down, the one you taught me, now I just have to get you! (you shouldn't have taught me-- too late now)

Rhinoceros?? Rynorsin?, Rhynursen ?? I believe it was Rynerson (Michael). Now tell me, does this come from "Reinersohn" which means "son of the purer" in German??! If so, something must have gone wrong somewhere down the line!! just kidding dude. Thanks so much for all the Proengineer and protomachine help. And of course, I developed the new CIP strategy using the samples that you had given me a long time ago. (read section 3.3.2 in this thesis if you're interested in finding out what we coinvented!) Leb' wohl!

Jim Serdy, thanks for going through the dehumanizing nine-hour ordeal of manually spreading powder with me to build those z bars... Also thanks for putting up with my incessant "materials related" questions and ... for being such a great story-teller. You're really the ultimate walking idiom/phrase book! (I look forward to getting my personal copy of the "Hagia Sophia!")

David Brancazio, thanks for always being so approachable and ready to help. The checker bars could not have been printed without your last minute help.

Jain Charnnarong and Won Bang, thank you guys for the anisotropy data, and all the help in file preparation and so on.

Steve Michaels, Jim Bredt, Alain Curodeau, thank you for the all the important advice I received from you.

Last but not least, I want to thank my friends Alkan, Binnur, Daniel, Deniz (Ertas), Dicle, John Lin, Kaori, Martin, Mete, Paco, Sridhar, Tamer, Tarun, Tumkan, Vidya, Vivek, and Zeynep for all the support and fun times together.

I wanted to write a message for each one of you but I really really really don't have any time left. My plane is leaving in 16 h and I have so much to do before then!!!

This thesis is dedicated to my mother Semra (aniiiiicim!), my father Cengiz (Cingoz), my brother Bogac (poker suratli Bobusko), and my sister-in-law Idil (sisko Idisko). I never would have completed it if it weren't for their unwavering support and trust.

CONTENTS

LIST OF FIGURES

LIST OF TABLES

CHAPTER 1

INTRODUCTION

Three-dimensional printing is expected to produce parts with anisotropic characteristics by virtue of the additive nature of the process. The knitting between primitive elements will be different along different directions, leading to strength and shrinkage anisotropy. The incentive to study the effects of print style on strength anisotropy has originated from studies done on investment casting molds. A modification of the simple raster scan print style was found to lead to much improved green strengths and to prevent breakage of molds during metal casting [Charnnarong]. Another modification to the print style, namely the implementation of triangular deflection of droplets (described under print styles in section 3.2.1) was observed to prevent splits during debind and sinter of metal parts, presumably by improving stitching along the slow axis. These two findings provided the motivation for verifying the existence of similar effects in the case of structural ceramics. The spray dried alumina-acrysol system was chosen for the current study.

The purpose of this thesis was to first determine the extent of green and fired strength anisotropy in structural ceramics parts fabricated via 3DP. To this end, the green and fired strength of long rectangular bars oriented along the three orthogonal axes of the 3D printer, i.e. the fast, slow, and z axes, were determined by four-point bend testing.

These results, along with shrinkage measurements revealed that green strength anisotropy was indeed an issue for current system. The goal was then to investigate the effects of varying a number of printing parameters, known collectively as the "print style," on the mechanical and microstructural properties of both green and fired parts. These parameters include the layer height, the line spacing, line arrangement, binder flow rate, and proportional deflection. This study was done in an effort to determine the potential benefits of print style modification as a means to the end of reducing the size and number of defects arising during the 3DP step. The simple linear raster scan style is compared with two different print styles, namely the staggered and the checker styles. Microstructural examination and four-point bend testing of green and fired bars prove that print style does have an effect on microstructure and strength.

In addition to the results of print style related experiments, this thesis reports mechanical strength data for 3DP-derived structural ceramics parts (Table 2.1) and describes how the current Cold Isostatic Pressing (CIP) technique was modified to allow CIP of complex shapes with hollow interiors (sections 3.3.2 and 4.2).

CHAPTER 2

BACKGROUND

2.1 Advanced Structural Ceramics

Ceramics are broadly classified as functional or structural depending on the type of application for which they are used. The former are used in applications that exploit their optical, electrical, and magnetic properties. Structural ceramics are used in applications that require excellent thermal and mechanical properties. They are expected to perform mechanical functions that demand high mechanical integrity at elevated temperatures. High strength-to-weight ratio, wear resistance, corrosion resistance, and high thermal shock resistance are among the major requirements. The most important examples of structural ceramics are materials that are based on alumina, zirconia, silicon nitride, and silicon carbide.

Nearly all experiments for this thesis have been performed using Al_2O_3. This ceramic material is used in a wide variety of materials-processing technology applications (textile guides, nozzle inserts, cutting tools, milling media) and electrical applications (spark plug insulators, electronic substrates, electrical insulation).

2.2 Processing of Advanced Structural Ceramics

Classical ceramics are processed from natural raw materials. Advanced structural ceramics, on the other hand, are manufactured from chemically processed materials.

Alternative manufacturing methods such as sol-gel processing, direct melt oxidation, and impregnation of fiber structures are currently being explored. However, advanced ceramics have traditionally been produced through the classic powder processing methods described below.

2.2.1 Powder Synthesis

The starting powders must be pure in terms of foreign particles for a structural ceramic component to have the desired reliability and high strength. They should also be free of hard agglomerates. Hard agglomerates are known to result in defects, and thus reduce the strength of the final product. The starting powder particles should be uniform, roughly spherical, and of a fine size, typically submicron, in order for a uniform, fine-grained final microstructure to be achieved. Alumina powder for structural ceramics is manufactured through one of four processes: the Bayer process, thermal decomposition of ammonium-alum, hydrolysis of aluminum alkoxides, and treatment of aluminum flakes by electric power discharge in water (Iwatani process) [Gauckler, 1988]. These processes are capable of yielding powders of varying fineness, and Na_2O impurity levels. The Reynolds RC172-DBM used for in our study was MgO doped Al_2O_3 synthesized by the Bayer process. MgO is commonly added to Al_2O_3 as a grain growth inhibitor.

2.2.2 Powder Processing

The powder must be prepared for the subsequent forming method once it has been synthesized. A polymer-ceramic mixture of high (up to 30 vol%) polymer content is

prepared for plastic-forming methods such as extrusion and injection molding. Fine ceramic powder is dispersed in a liquid vehicle, either water or an organic solvent in slip casting and tape casting. Small amounts of organic stabilizers (or deflocculants) are added to prevent the formation of particle aggregates which can lead to structural faults in the final product. Appropriate amounts of binder and plasticizer (~ 6 vol% of each) are added also in the case of tape casting. The most widely used forming process is dry pressing. This process works best with highly flowable, controlled granules. Such granules are often prepared by spray-drying. A small amount of binder is added to the slurry to be spray dried. The binder serves the purpose of holding together the ceramic particles that make up individual spray-dried granules, and of improving the compaction behaviour of granules. A plasticizer is commonly added to ease deformation of granules during the subsequent pressing stage. The spray-dried alumina powders used in our experiments were produced in-house.

2.2.3 Forming Methods

Several forming methods exist for consolidating ceramic feed material into a coherent body having a definite shape and microstructure. The goal of all forming methods is to produce a homogeneous green body with high green density. The green body is generally required to be about 60% of theoretical density for ceramics that sinter by solid-state diffusion. Green densities as low as 30% would have been sufficient to ensure normal sintering at the sintering temperature (= 1650°C) used in the present work. Green densities lower than about 30% would fall into the subnormal regime [Bruch,

1962] where sintering does not occur. These issues will be discussed further in section 2.2.5. Some of the conventional forming methods are briefly described below. The uniqueness of 3DP as a viable forming method will be described in section 2.7.2.

Injection Molding/Extrusion

Injection molding is a plastic forming technique whereby a ceramic-polymer mixture is injected into a mold by a plunger, using a combination of heat and pressure. The viscosity of the plastically deformable mixture is required to be low for proper filling of the mold and for prevention of air bubble entrapment. Extrusion, a similar plastic-forming process, is used to produce long, uniform cross section parts. Extrusion dies are open at one end in contrast to injection molding dies. Clay bricks, tiles, and pipes, as well as monolithic cordierite honeycomb structures for catalyst supports have been fabricated by extrusion.

Slip Casting

Slip casting involves pouring a ceramic slip into a porous mold, commonly a gypsum mold with 40-50% porosity, which absorbs liquid and deposits solid material on the mold walls. Excess slip is drained off. The cast is then removed and fired. The quality of a cast generally depends on three factors. First, the slip must be stable so that deposition occurs evenly on the mold walls. Second, the solids content must be high (~70 wt%) to improve drainage rate. Lastly, as with injection molding, slip viscosity must be low enough so that the mold may be filled easily, and air bubble incorporation

into the green body prevented. Slip casting has been used for manufacture of tableware, sanitaryware, crucibles, tubes, thermocouple sheaths, and gas turbine stators.

Dry/Isostatic Pressing

Pressing is used for the simultaneous compaction and shaping of soft, controlled agglomerates in a rigid die (dry-pressing), or a flexible mold (isostatic pressing). Parts thicker than 0.5 mm and parts with surface relief in the pressing direction are dry-pressed using hardened metal punches. Products fabricated by dry-pressing include various fine-grained technical aluminas such as spark plugs, engineering ceramics such as cutting tools, ceramic tile and porcelain products, coarse-grained refractories, grinding wheels, and structural clay products.

Pressure, and consequently density gradients are set up within a compact during dry-pressing due to die wall friction. Isostatic pressing, or isopressing, offers one way of reducing this friction effect, thus minimizing density gradients within the green body. Isopressing involves pressurizing powder filled flexible rubber molds in liquid pressure chambers. This method is used to produce shapes with relief in two or three directions. A variation of the so-called wet bag technique, which is commonly practised in industry for pressing complex shapes of various sizes and large refractories, was used for our specimens.

Tape Casting

Nonuniform density, nonparallel faces, and breakage become important limiting factors in dry-pressing of articles that are thinner than 2 mm. Tape casting, a continuous, high-productivity process, is *the* viable alternative for the manufacture of flat, smooth, thin (0.01-1 mm) ceramic substrates of uniform density. A film of controlled thickness is formed when a slurry flows down an inclined substrate, or under a blade onto a supporting surface. The cast film is dried to an elastic, leathery state, and cut to the proper handling width. A puncher is used to shape the dried film. This process is used to manufacture substrates for multilayer ceramic electronic packaging, multilayer titanate capacitors, piezoelectric devices, thick and thin film insulators, ferrite memories, and catalyst supports.

2.2.4 Compaction Behaviour of Spray Dried Granules

Plotting relative green density vs. log (punch pressure) for spray-dried granule compacts reveals that compaction of spray-dried granules occurs in three distinct stages [Youshaw, 1982]. In stage I, granules might rearrange some to give a higher than fill density packing. Stage II typically begins at about 1 MPa. During this stage, depending on the amount and plasticity of the binder, granules fracture or deform, filling up intergranular voids. Of the three stages, the highest extent of densification occurs in this stage. Large intergranular pores, as well as interfaces between softer granules are mostly eliminated. Interstices between harder granules persist into stage III, which starts at about 20 MPa. During stage III, particles rearrange a bit further into a denser packing configuration, increasing the homogeneity of the powder mass.

Intergranular pores have a negative effect on the densification of green compacts during sintering and on the bending strength distributions of the sintered bodies. These pores must collapse completely to produce highly reliable, high-strength ceramics. This is discussed in further detail in the following section.

2.2.5 Sintering-- Pore Elimination

Sintering refers broadly to the changes in grain/pore size and shape that ceramic (or metal) particles in contact undergo when heated to high temperatures. The elimination, or at least minimization of porosity by the sintering process is essential in ceramics if properties such as strength [Carniglia, 1972; Davidge and Evans, 1970], translucency [Peelen and Metselaar, 1974], and thermal conductivity are to be maximized. Experimental data suggests that strength, for instance, is decreased nearly exponentially with porosity. This is because residual pores in a fired part increase the amount of stress experienced by that part. They do so not only by reducing the effective load bearing cross sectional area, but also by acting as local stress concentrators. The stress is increased by a factor of two in the vicinity of an isolated spherical pore.

Densification, or consolidation of a porous green compact to full density by pore shrinkage, is accomplished by solid phase or liquid phase sintering. The driving force for sintering is the decrease in total free energy of the system associated with replacement of solid-vapor interfaces by lower-surface-energy solid-solid interfaces, namely grain boundaries [Smith, 1948; Coble, 1959]. This is achieved by the transport of material away from the contact area between two particles into the necks around this area.

Regardless of whether this occurs by bulk diffusion, grain boundary diffusion, or through a liquid phase concentrated at the grain boundaries, the transport distance will be smaller, and the sintering rate will thus be higher for smaller grain sizes.

Stages of Sintering

Sintering can be conceived as a three-stage process [Coble, 1961 (I)]. *The initial stage* is where necks form at the contact points between particles. This is accompanied by interparticle shrinkage of a few percent [Kingery and Berg, 1955; Coble, 1958]; the relative density of a typical powder compact will increase by about 20% during neck growth. No grain growth occurs, i.e. the boundaries between the single-crystal particles do not migrate during the initial stage. This is because the solid-vapor surfaces diverge from the grain boundary surfaces at an acute angle. Migration of the boundary would result in a significant increase in grain boundary area given this particular geometry and thus be energetically unfavorable. The termination of the initial stage is marked by the onset of grain boundary migration, i.e. grain growth, as the transport of matter to the necks rounds and blunts them, relieving the geometrical restraint.

A significant amount of grain growth and pore shape change takes place before *the intermediate stage* begins, forming equilibrium dihedral angles at the pore-grain boundary intersections. The intermediate stage itself is characterized by a shrinking continuous, interconnected pore phase, intersected by grain boundaries.

The final stage begins as the continuous pore phase breaks up into isolated pores along grain boundaries. These pores can generally be made to shrink to zero size in a

stable fashion hereafter. However, discontinuous, (a.s.a abnormal, or exaggerated) grain growth may occur, leading to the entrapment of porosity inside grain interior. During discontinuous grain growth, grain boundaries move on across pores and reform on the other side. Pores entrapped thus will generally persist to high density since they must rely on lattice diffusion for closing off, which is a relatively slow transport mechanism. Densification can only proceed at a reasonable rate if the sources and sinks for the associated diffusion process are kept close together. The pores must remain attached to or at least close to grain boundaries if full density is to be attained [Burke, 1957; Burke and Rosolowski, 1974]. Thus, discontinuous grain growth must be actively suppressed during the final stage of sintering for the attainment of close to theoretical density [Coble and Burke, 1963]. This is achieved by the addition of grain growth inhibitors. In the case of Al_2O_3, for example, MgO is used for this purpose [Coble, 1961 (II)].

Porosity is never ideally distributed in experimental green samples. As a consequence, a distribution of pore sizes will generally exist as the intermediate stage of sintering is entered. The pore concentration variations will generally persist to the final stages of sintering as a result of the slower elimination of larger pores. Large pores in a poorly compacted powder tend to be thermodynamically stable or even grow [Rhines, 1950]. A ratio of pore diameter to grain diameter greater than 1.5 is sufficient for pores to grow in pure alumina [Kingery et al, 1976]. Carbone and Reed (1978) have also found that a broad range of pore sizes distributed inhomogeneously leads to poor sintering behaviour. They report that a uniform distribution of pores up to about one particle size is required for optimum sintering characteristics.

Subnormal/Normal Sintering Regimes

The relationship between green and final density in the MgO-doped alumina system has been studied extensively [Bruch, 1962; Greskovich, 1972]. Bruch defines two sintering regimes based on the variation of the time exponent with temperature and green density in an empirically derived sintering kinetics equation. The region in the green density-temperature space where the time exponent is independent of these two parameters is called *the normal sintering regime*. This behaviour is observed at higher green densities and/or higher temperatures. The magnitude of the time exponent decreases with decreasing green density and/or temperature in the so-called *subnormal sintering regime*. An important observation made by Bruch is that for compacts within the normal sintering regime, green density has a profound effect on the rate coefficient, viz. the coefficient increases with green density. Thus, lower density compacts can "catch up"with higher density compacts, i.e. achieve approximately the same final density within a given period as higher density compacts.

The consequences of having higher and lower density regions within a uniform packing density green matrix were studied by Lange and Metcalf (1983). They observed that for specimens containing lower-density agglomerates, circumferential cracklike voids were formed at the agglomerate/matrix interface. Similar results were obtained for our specimens. Uncollapsed spray-dried granules have a lower green density (~ 50% theoretical density) than the surrounding collapsed powder mass (~ 60% theoretical). The range of sintering variables in the present work (local green density = 50-60%, sintering

temperature = 1650°C) were such that sintering occurred strictly in the normal regime as defined by Bruch (1962). Thus, the lower-density uncollapsed or partially collapsed granules presumably sintered at a faster rate than the surrounding matrix, attaining approximately the same final density. Due to the differential shrinkage, intergranular pores were exaggerated. These results are discussed further in section 4.1.1.

2.3 Fracture Strength of Structural Ceramics

No metal can be used under mechanical load at temperatures above 1100°C without the use of some sort of cooling system [Gauckler, 1988]-- for such applications, advanced structural ceramics stand alone as the materials of choice. Ceramics have great thermal and chemical stability, high hardness and wear resistance owing to their strong ionic and covalent interatomic bonds. However, these bond characteristics preclude the plastic behaviour that is normally associated with metals, causing them to undergo brittle fracture.

Crack initiation is the critical stage of the rupture process in brittle materials like ceramics. The crack begins to propagate under the right stress conditions once it is initiated since there is no large energy absorbing process like in ductile materials. Grain boundaries in polycrystalline ceramics can act as obstacles that force the crack to change direction at a boundary, increasing fracture stress by a factor of 2 to 4.

The part fails when the crack finally grows above a certain critical size. Crack propagation occurs when the decrease in stored elastic energy associated with the extension of the crack exceeds the energy required to form the new fracture surfaces.

This energy balance argument first formulated by Griffith leads to the following equation for fracture strength:

$$\sigma_F = \frac{K_c}{(\pi c)^{1/2}} \tag{2.1}$$

where σ_F = fracture stress

K_c = fracture toughness

c = crack size

Equation 2.1 clearly suggests that there are two possible ways of increasing the strength and reliability of structural ceramic components. The first of these is to reduce the size of (both process and machining-induced) defects, which act as stress concentrators and lead to breakage at relatively low stresses. The second approach is to increase the fracture toughness of the material through techniques such as transformation toughening (e.g. Al_2O_3-ZrO_2), the introduction of a second phase (e.g. SiC-TiB_2), fiber and whisker reinforcement (e.g. Al_2O_3-SiC), or grain boundary engineering (e.g. Si_3N_4/YAG) [Gauckler, 1988]. The present work focuses on eliminating or at least reducing the number and size of processing related defects, specifically those introduced during the three-dimensional printing step (see section 2.5.4 and 2.6 about 3DP).

2.4 Mechanical Testing of Structural Ceramics

The maximum tensile strength of ceramics is ordinarily not determined through tensile testing due to the inherent difficulty in gripping brittle specimens without breaking them. Instead, three-point and four-point bend testing are widely used. The maximum tensile stress that the specimen can withstand, namely its Modulus of Rupture (MOR) is largely determined by the size of flaws present in the stressed region of the specimen, which act as stress concentrators. The entire volume of the specimen is under maximum stress in the case of tensile testing. The maximum stress is restricted to a line on the surface of the specimen in three-point bending, and a planar region in four-point bending [Nunomura, 1989]. Consequently, for the same specimen shape and size, the probability of finding a supercritical flaw in the stressed region is highest in tensile testing, lower in four-point bending, and lower still in three-point bending. The mean value and variability in strength in bend testing is correspondingly higher compared to tensile testing.

2.5 Solid Freeform Fabrication (SFF)

Solid Freeform Fabrication, otherwise known as rapid prototyping or desktop manufacturing, can be defined as the production of freeform solid objects directly from a computer-aided drawing (CAD) without the use of part-specific hard tooling, dies, or molds. A variety of SFF techniques have been developed in recent years that use radically different techniques and materials. The common aspect of these systems is that they construct parts or prototypes through additive laminated building processes. A three-dimensional representation of the part is sliced into two-dimensional cross sectional layers. These slices are then used to guide the SFF machine in building the part on a

layer-by-layer basis. Presented below is a brief description of those SFF techniques that have been demonstrated in the manufacture of structural ceramics.

2.5.1 Laminated Object Manufacturing (LOM)

Laminated Object Manufacturing [Griffin, 1994] is capable of building parts out of paper, plastic, metal sheet stock, or ceramic tape. A sheet of material is rolled in over the work area. A computer-guided laser cuts out a cross section of the part and cuts the remaining portions into tiles to facilitate part removal. A new sheet is laminated to the previous sheet by passing a hot roller to activate a previously applied adhesive layer. This process is repeated until the full part emerges.

2.5.2 Selective Laser Sintering (SLS)

Selective Laser Sintering is commercially available for use with polycarbonate, PVC, and wax powders. Parts have been fabricated from metal and ceramic powders also. SLS is based on spreading uniform layers of powder material much like three-dimensional printing (3DP). A CO_2 laser then scans the powder bed in computer-specified regions. The beam intensity of a laser can be adjusted so as to melt or sinter together the powder material. This spreading-scanning cycle is repeated until the part is completed.

Direct sintering of ceramic materials with SLS requires the use of high laser energies (~1000 cal/cm^2). However, even at these high intensities, completed parts hardly hold together because of the high thermal gradient and rapid heat dissipation

involved. Low melting temperature inorganic and organic second phases have been used to obtain green alumina parts [Subramanian et al, 1994].

2.5.3 Stereolithography

Stereolithography has traditionally been used to make plastic parts. A UV laser scans a bath of acrylate liquid causing it to photopolymerize in selected regions. The cured part is supported usually from underneath by a flat surface attached to an elevator which lowers once the layer is completed. The liquid polymer flows over the cured part, and the laser scans the next cross-section. Attempts have been made at adapting Stereolithography to produce ceramics. Alumina slips consisting of 45-55 vol% ceramic powder have been dispersed within a UV-curable aqueous acrylamide solution [Griffith, 1994]. Single layer parts have been constructed using this new technique.

2.5.4 Three Dimensional Printing (3DP)

3DP is a solid freeform fabrication technique that utilizes ink jets to place binder droplets in a computer-specified pattern onto layers of powder material. The ability of 3DP to fabricate parts out of materials as diverse as polymers [Borland], metals [Michaels, 1992], ceramics [Yoo, 1993], glass, and glass-ceramics [Nammour, 1995] has been demonstrated.

A pile of powder is dispensed at the edge of the piston which supports the powder bed. A spreader rod then pushes the powder across the piston, spreading it in a thin layer ($\sim$ 150 μm). The spreader rod is usually vibrated in the vertical plane at about 400 Hz.

Most powders (e.g. 30 micron alumina and metal powders) are dispensed automatically from a reservoir situated above the machine. Powder layer generation techniques have been described elsewhere [Lee, 1992].

Once the spreading of the powder layer has been completed, it is raster scanned by the printhead. Liquid binder is delivered through a continuous-jet type ink-jet printhead. The continuous stream of binder that passes through a nozzle with a 45 μm orifice is made to break up into small droplets by a piezoelectric disc attached to the nozzle vibrating at about 60 Hz. Droplets are then selectively charged as they pass through a capacitor. A high voltage electric field deflects the charged droplets, directing them onto a "catcher" so that the unprinted binder may be recycled. Uncharged droplets pass undeflected through the deflection cell, falling vertically into the powder bed. Thus, the powder bed gets selectively glued together by the binder droplets. The spreading-printing sequence is repeated until the full green part emerges. Figure 2.1 shows the so-called fast, slow, and z axes on a three-dimensional printer.

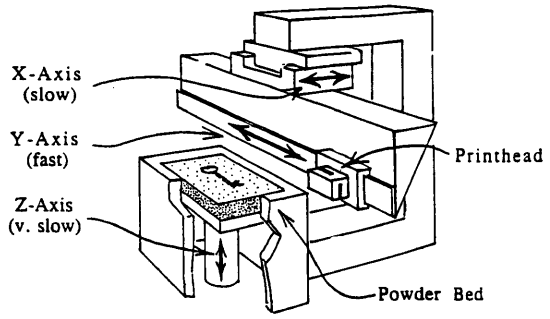

Figure 2.1 Schematic diagram showing the fast, slow, and z axes on a three-dimensional printer.

2.6 Process Physics of Three-dimensional Printing (3DP)

2.6.1 Single Drop Primitives

The smallest building block in a 3D-printed part is called a primitive, and is an agglomerate of powder particles (or granules) formed by a single binder droplet. Powder particles are pulled together into spherical agglomerates in response to the binder liquid surface tension forces. The physics of primitive formation has been studied extensively [Bredt, 1995]. The single drop primitive size is determined by various factors such as binder drop chemical composition and size, powder chemical composition and size, layer thickness, powder bed density and surface tension. For example, a 75 μm drop of colloidal silica printed on a 175 μm thickness of 30 μm alumina powder will form a 125 μm drop primitive.

Drying of the binder droplet will typically be accompanied by rearrangement of the powder particles leading to further densification. Indeed, the packing density of primitives composed of 325 mesh alumina powder is 1.8 times higher than the rest of the powder bed [Lauder, 1992]. Thus, the primitive represents a defect since its formation results in an inhomogeneity in the packing density of the powder. The spray dried granules used in this study are certainly prone to rearrangement upon contact with the liquid binder since they have high flowability, i.e. low cohesive strength.

2.6.2 Lines

The simplest print design places binder droplets on a straight line to form the next substructure in the hierarchy, the printed line. The 75 μm droplets in the example above, when overlaid on each other every 20 μm, will form a 200 μm wide line [Sachs, 1994]. This highly linear arrangement ensures good knitting between primitives within a printed line along the fast axis. However, this occurs at the expense of poor knitting along the slow axis. Defects appear between pairs of lines as a result of the ballistic interaction between the powder and the binder combined with powder rearrangement effects [Lauder, 1992]. "Triangular deflection" is currently being used to help alleviate this problem. This print pattern is described in greater detail in section 3.2.1. The specific observations pertaining to line formation in spray dried powder beds are given at the end of section 4.1.2.

2.6.3 Layers

Knitting between individual layers can be improved either by reducing the layer thickness, and/or by modifying the print style. Cylindrical printed lines are stacked right on top of each other in the simple linear raster print style. An alternative approach (staggered style) reduces the layer thickness and staggers the lines so as to achieve a more closely packed line arrangement. This approach was first demonstrated to reduce strength anisotropy in bars printed with coarse alumina powder and silica binder [Charnnarong]. The present work corroborates this effect for the spray dried alumina - acrysol system.

There are other important printing parameters besides print style and layer thickness, such as binder saturation in the powder bed (controlled by the printhead speed

along the fast axis, the binder flow rate, the powder bed packing density, line spacing, and layer thickness), as well as materials parameters, such as the wetting characteristics of the powder. These also play an important role in determining the defect structure and mechanical strength by affecting how the printed lines rearrange themselves and how the binder gets distributed within the printed part.

This thesis discusses the extent of anisotropy found in green as well as fired structural ceramics printed using three different print styles. The effect of print style alone on strength anisotropy and microstructural properties was demonstrated by varying the print style while keeping other parameters constant (or by factoring out the effects of other parameters).

2.7 Strength and Anisotropy in Structural Ceramics via Conventional vs. SFF Techniques

2.7.1 Conventional Methods

The values reported for room temperature bending strengths of polycrystalline 98% bulk density alumina vary as a function of porosity in the range from 200 to 500 MPa depending on experimental conditions and material composition.

Another source lists strengths for different grain sizes [Cook, 1985]. The average strength for alumina with a 3 μm grain size is 488 MPa; for 11 μm, 400 MPa; and for 25 μm, 302 MPa. The grain size in our samples is ~4-7 μm, which corresponds to ~450 MPa.

A commercial grade alumina is reported to have bending strengths of 379 MPa. (Data from product data sheet for AD995 (99.5%) alumina, data sheet 7164C FP 20K 2/89, Coors Ceramics Co.)

2.7.2 Solid Freeform Fabrication Techniques

The only solid freeform fabrication (SFF) technologies that have demonstrated structural ceramic parts are LOM, Stereolithography, SLS, and 3DP.

LOM

Strength results for dry-pressed and LOMed bars have been compared [Griffith, 1994]. Flexural strength varied ~ 3% with direction in dry-pressed bars (w/ 0.4% open porosity). Bars where the tensile stress was applied parallel to the pressing direction broke at ~336 MPa. Average strength was 325 MPa for stresses applied perpendicular to the pressing direction.

Flexural strengths of about 310 MPa were reported for LOMed alumina bars with 1.0% open porosity. Strength anisotropy in this case was statistically insignificant. The test direction parallel to the lamination direction produced an average of 314 MPa; the perpendicular test direction produced 311 MPa.

Stereolithography

Ceramic green bodies have recently been created through Stereolithography of dispersions of alumina slip (45-55 vol% solids) within a UV-curable aqueous acrylamide

solution. Only one layer thick green parts (300 μm) have been built so far. However, initial results are promising.

SLS

Fully dense monolithic structural ceramics have not been demonstrated for this technique. However, SLS was done on 100 μm agglomerates of 2 μm Al_2O_3 particles mixed with polymer powder to construct alumina green samples [Subramanian, 1994]. Samples were built in different orientations. The green bend strengths revealed that samples built using shorter scan lines have higher strengths (~ 2 MPa). The anisotropy is due to the fact that, for shorter scan lines, there is less time for heat dissipation between two consecutive scans. The process physics is quite different than both LOM and 3DP. However, in both SLS and 3DP, anisotropy is a result of the additive nature of solid freeform fabrication.

3DP

3DP has two main advantages over conventional powder forming methods. Fabrication of complex shapes through powder molding processes like injection molding involves forming a heavily plasticized powder mass against a mold. Depending on the shape and size of the mold, differential shear forces may develop during the process, resulting in inhomogeneity in powder packing, which in turn leads to distortion upon firing. In contrast, each layer in the 3DP process is prepared in the same way so that the particular shape or size of a part has no effect on distortion. Secondly, a 3D-printed

ceramic green body typically contains 2-3 wt% binder unlike injection molding, where up to 30 v/o polymer is required to plasticize the powder. Thus, 3DP is potentially unrestricted in its capability to manufacture parts having large dimensions unlike injection molding where cracking problems during binder burnout preclude manufacture of thick cross section parts.

The capability of 3DP to fabricate structural ceramic components has been demonstrated for several different materials systems. Prior to this study, a number of structural ceramic parts had already been fabricated out of fine alumina powder using the press-rolling spreading sequence and the linear raster print style. Bars constructed this way had average MORs of 324 MPa [Yoo, 1993].

Spray dried alumina powders were used for the current study. Fabrication of alumina bars involved three different print styles. The highest fired MORs (~400 MPa) were obtained using the so-called staggered style. Green strengths along different directions varied by a factor of 3. On the other hand, virtually no strength anisotropy was observed in fired bars.

Silicon nitride bars with flexural strengths of 570 ± 112 MPa were also fabricated. Concurrently, Zirconia Toughened Alumina (ZTA) bars with an average strength of 475 MPa were constructed by Yoo (1995). Flexural strengths of inceram infiltrated alumina parts prepared by Nammour averaged 205 MPa. These flexural strength results are summarized below in Table 2.1.

Type of Material	4-pt Bend Strength (MPa)
Inceram infiltrated Al_2O_3 [Nammour, 1995]	205
fine Al_2O_3 [Yoo, 1993]	324
linear raster Al_2O_3	340
checker Al_2O_3	340
staggered Al_2O_3	380
ZTA [Yoo, 1995]	475
Si_3N_4	570

Table 2.1 Demonstrated mechanical properties of 3DP-derived materials.

Finally, a wet deposition process is currently being developed by Khanuja for direct fabrication of structural ceramics. The process features spray deposition of slurries, building high green bodies that can be sintered directly to full density. It eliminates the need for the intermediate isostatic pressing step required in dry processing.

CHAPTER 3

EXPERIMENTAL PROCEDURE

3.1 Materials

The ceramic powder used in almost all of the experiments reported in this thesis was spray dried Al_2O_3. The mechanical strengths of parts made out of Si_3N_4 are included as well. The binder used was a diluted form of Acrysol WS-24 in all cases.

3.1.1 Binder

The binder used in all the experiments was a 6 vol% Acrysol WS-24 (Rohm and Haas Company, Philadelphia, PA) solution in water (99.9 vol% water, 0.1 vol% ammonia). Acrysol is an acrylic copolymer dispersion resin.

This formulation, originally optimized for submicron alumina powder [Yoo, 1993], was adopted successfully for all the spray-dried as well as the submicron powders used in this study.

3.1.2. Powder

Alumina

Spray dried alumina powder was prepared from submicron alumina powder (Reynolds RC 172 DBM) using an in-house laboratory scale spray drier. 2 wt%

polyacrylic acid (M_w = 240,000) was used as a binder. The resulting spherical spray dried granules had high flowability and a packing density of ~ 30% on spreading. Bulk density of granules varied from batch to batch, averaging about 47%. Fines, i.e. loose submicron particles, were sieved out in most cases. Granule sizes between 30 μm and 100 μm were used for printing.

Silicon Nitride

Si_3N_4 powder (grade M11; H.C. Starck, Germany), containing 6wt% Y_2O_3 (Atlantic Equipment Engineers; Bergenfield, NJ) and 6wt% Al_2O_3 (Baikalox type CR-30; Baikowski International Corporation, Charlotte, NC) as sintering additives was used to fabricate rectangular bars. The powder mixture was ball milled for 20 h in ethanol using ZrO_2 media. The slurry was air dried, crushed, and sieved to obtain agglomerates between 53 μm and 106 μm for printing. Spray-drying was not used in this case.

3.2 Sample Preparation-- 3D Printing

3.2.1 Alumina Bars and Lines

Three sets of rectangular bars (0.46x0.46x3.8 cm) were fabricated on the alpha-machine using three different print styles, namely the ***linear raster***, ***staggered***, and ***checker*** styles. Figures 3.1-3.3 show the distinctive features of these print styles. Each set of bars consisted of fast, slow, and z bars, with their long axes parallel to the three orthogonal axes of the 3D-printer (Figure 3.4). Four-point bend testing was performed on

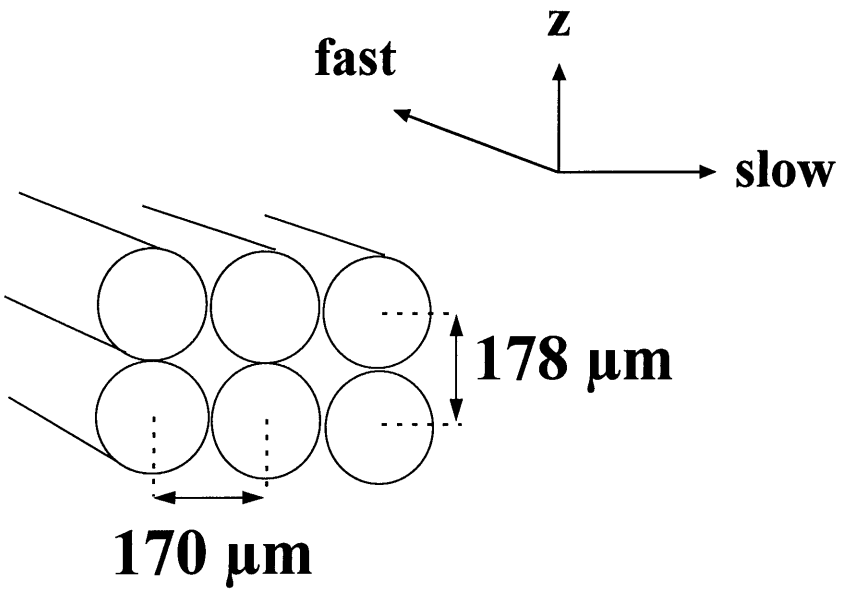

Figure 3.1 Lines are stacked right on top of each other in the linear raster print style. The dimensions that were used are indicated in this drawing.

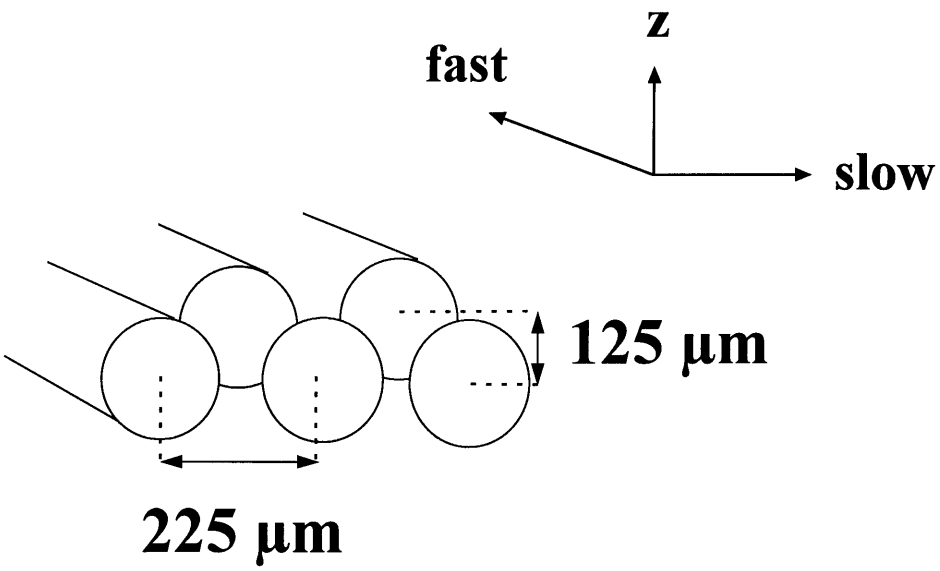

Figure 3.2 Line spacing is increased and layer thickness reduced in the staggered style. Lines are staggered in alternate layers to achieve higher packing.

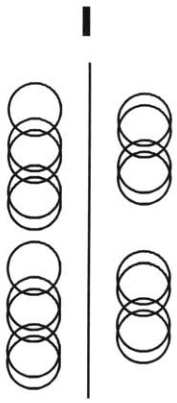

a) A single line

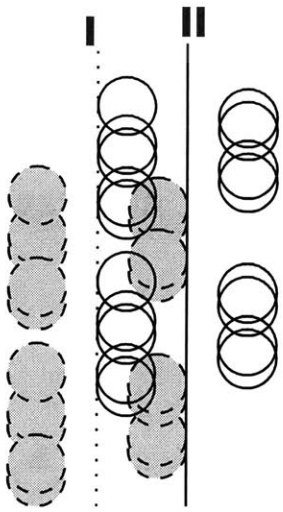

b) Two consecutive lines 250 microns apart

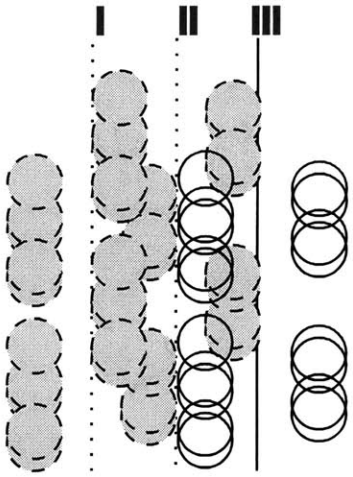

c) Three consecutive lines

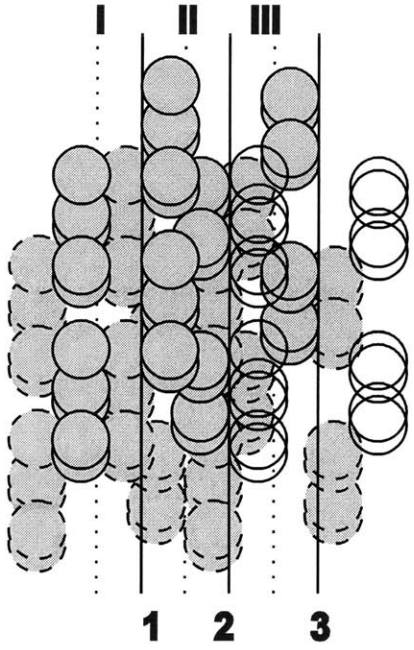

d) Two consecutive layers

Figure 3.3 This schematic shows consecutive lines and layers in the checker build style. The total deflection for a given line is 250 microns. Line spacing is 125 microns. I, II, III represent the centerlines of the 1st, 2nd, and 3rd lines in the 1st layer 1,2, and 3 represent the 1st, 2nd, and 3rd lines in the subsequent layer The empty circles are the primitives of the last line to be printed. The gray circles are the primitives of previous lines.

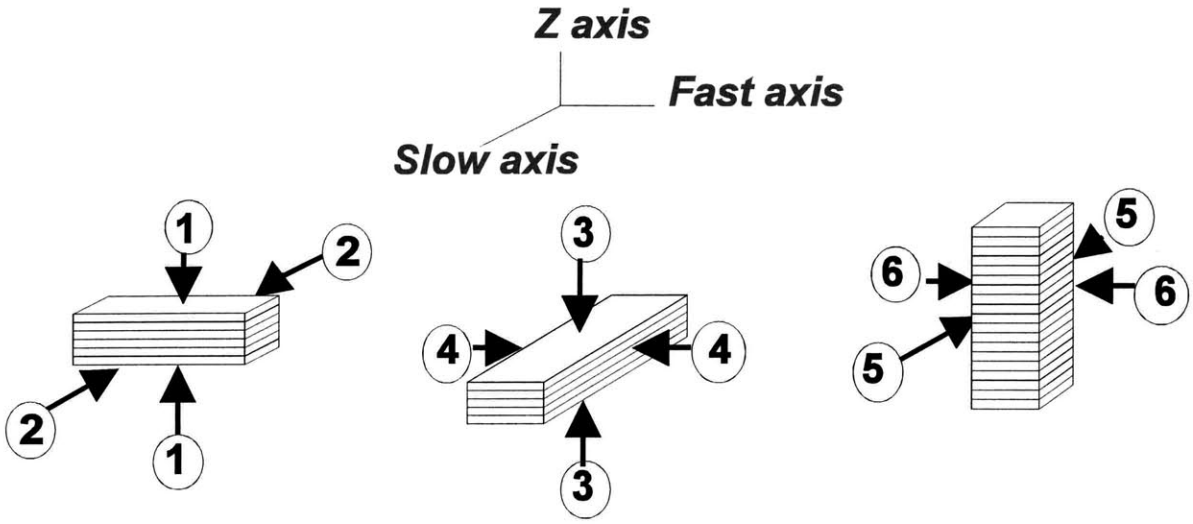

Figure 3.4 Fast, slow, z bars were all loaded in one of two directions

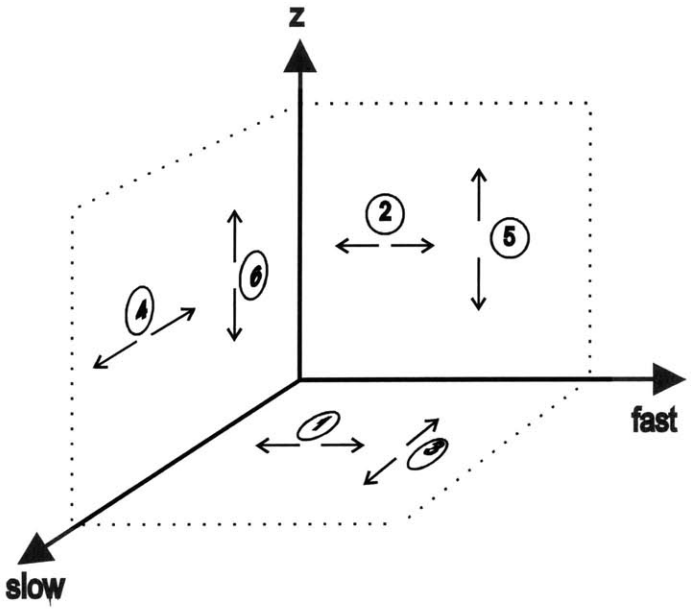

Figure 3.5 The extent of stitching in 3D-printed green parts was measured along two different axes in three different planes, creating six different tensile stress configurations The numbers correspond to the six loading directions shown in Figure 3.4

as-printed green bars in order to understand the effects of print style on the quality of stitching between primitives in different planes and along different directions. Each type of green bar was loaded in two different ways, creating a total of six distinct tensile loading configurations as shown in Figure 3.5. Such a distinction was not made in the case of fired bars. Fast and slow bars were always broken with the top surface (last layer to be printed) in tension while z bars were always broken with the front surface (formed by the last line in each layer) in tension.

Strategy

6 vol% Acrysol had already been established as the optimum binder formulation for printing on fine alumina powder [Yoo, 1993]. Higher concentrations (12 vol%) were found to lead to binder build-up between layers, forming interlaminar defects [Yoo, 1993]. The linear raster bars were thus fabricated by printing 6 vol% Acrysol. The other printing parameters that were used are tabulated in Table 3.1 in Section 3.2.3. The saturation values in this table assume the intragranular porosity within spray dried granules to be completely accessible by the binder solution.

The fracture surfaces of linear raster bars that were isopressed (240 MPa, 80°C) and then fired revealed long linear defects that were clearly formed during the 3DP step. That these defects were 3DP-induced was confirmed by a compaction experiment where loose spray dried alumina powder was post-processed and fired in the same exact way as the printed bars, i.e. evacuated, WIPed, and fired according to the recipes given in Section 3.3.1. The thickness of the loose powder was made to approximate the thickness of the

green bars so that any thickness related effects would be eliminated. The fracture surface of this sintered compact revealed no defects, proving that the defects observed in the bars were in fact 3DP-induced.

There are several ways in which 3DP can cause the kinds of defects observed in fired linear raster bar fractographs to arise. One possible cause is excess binder accumulation between granules, preventing them from merging together. Excess binder can get deposited between granules as a consequence of too high a printed binder saturation and/or nonhomogeneous distribution of binder solution within intergranular voids. A pore will then be left in place of the excess binder during the debind. Such pores will typically be large enough to persist during the subsequent sintering process. Lowering the amount of binder printed per unit volume can solve the problem in this case. The defects, however, can also be caused by the rearrangement of granules upon contact with the binder. This can result in the formation of large voids between lines, and layers that are difficult to close by isopressing and sintering. Improving the print style should be expected to have a positive effect on the final defect structure in this case. Staggered style printing attempts to solve the problem in one step by incorporating both of these solutions.

The staggered style, demonstrated to give better stitching compared to linear raster in the alumina-silica system [Charnnarong, 1994], was used to fabricate the next set of bars. The same binder solution (6 vol% Acrysol) was printed at 20% lower saturation. Thus, these bars contained 20% less printed binder per unit volume than the linear raster bars. Also, the spray dried granules used in this case were 1.3 to 1.6 times larger. Either

one of these changes alone may have led to the observed 10 % increase in fired bar strength and the reduction in defect size and frequency. It is much more likely, however, that each played a role as a contributing factor. This will be discussed in greater detail in Section 4.1.1. One practical observation was that green bars were still more than sufficiently handlable even though they contained 20% less Acrysol than the first set of linear raster bars.

The checker style printing run used the same binder saturation and granule size as the staggered bars so that the effect of print style alone could be studied.

Finally, isolated single, double, and quadruple adjacent line sequences were printed on the protomachine. Three line spacings were tried, namely 178 μm, 203 μm, and 229 μm. The flow rate was 1.2 cc/min; the fast axis speed was 165 cm/s. The lines were examined in their unretrieved form in the powder bed using a Nikon SMZ-U type stereomicroscope. This study was done to quantify the extent of ballistic interaction between the binder and the powder and to understand the phenomenon of line formation in the spray dried powder- acrysol system.

Print Styles

Linear raster style

The simplest print style, i.e. the linear raster scan, stacks cylindrical printed lines directly on top of each other as shown in Figure 3.1. The linear raster parts for this thesis were all printed prior to the implementation of a modified version of the style involving

"triangular deflection" of droplets. The modified version has been in use since October of 1994 for printing metal parts. Droplets are deflected symmetrically towards either side of the centerline formed by undeflected droplets. The number of droplets that land at a certain distance away from this centerline decreases linearly with the distance. Thus, a triangular distribution of droplets is obtained around the centerline. The extreme points of this "triangle" coincide with the centerlines of the two adjacent lines on either side. Adjacent lines overlapping in this manner give a constant number of droplets along the length of the slow axis. This style has been demonstrated to prevent splits during debind and sinter of metal parts, presumably by improving stitching along the slow axis. The triangular deflection pattern represents just one example of a whole array of possible "pattern printing styles" achievable through proportional deflection. The one pattern printing style used in our experiments was the checker style, a "patternized" version of the staggered style. These two were the only other styles that were used in this study besides the nonpatternized version of the linear raster style and are described in the following sections.

Staggered style

This style had already been demonstrated to reduce strength anisotropy in bars printed with coarse alumina powder and silica binder [Charnnarong, 1994]. Investment casting molds printed this way were found to be less prone to cracking during metal casting. Thus, it was chosen as a first modification of the simple linear raster scan. The staggered style reduces the layer thickness and staggers the lines so as to achieve a more

closely packed line arrangement (Figure 3.2). The staggered style increases the line spacing in addition to reducing the layer thickness. Consequently, adjacent lines are separated by regions of unprinted powder and prevented from fusing together. The subsequent layer is then formed by printing over these unprinted regions. This method is believed to influence powder rearrangement in such a way that printing-induced defects are minimized.

Checker style

The checker style extends the idea of staggering of printed elements and leaving unprinted regions one step further. It applies it on an even smaller scale, i.e. within the printed line. It is a pattern print style based on the staggered style. It keeps the same layer height and line spacing. However, instead of printing continuous lines, it prints dashed-lines, i.e. a series of line segments separated by unprinted regions. Furthermore, proportional deflection is used to "smear out" each line segment into rectangular "unit cells." The next line prints the same pattern, staggered in such a way that the unit cells fall next to the regions left unprinted in the previous line. These two patterns are alternated until the layer is completed, forming a checkerboard pattern. Finally, the layers are staggered so that a checkerboard pattern is formed in the fast-z and slow-z planes as well. Among the parameters that can be varied in this style are the size of the unit cell, and the ratio of printed to unprinted droplets. The average deflection from the centerline for 8 jets was 103 μm in either direction with a standard deviation of 16 μm for this particular printing run. The ratio of printed to total number of droplets was 0.692. The

line spacing was 202 μm. Each unit cell consisted of about 9 droplets arranged as shown in Figure 3.3(a). A schematic of the steps involved in building two consecutive layers is shown in Figure 3.3. The deflection and printed line thickness are both taken to be 125 μm in this drawing.

3.2.2 Alumina Pre-ignition Chambers

Nine pre-ignition chambers (prechambers) were printed with spray dried alumina and 6 vol% Acrysol using the staggered style. The staggered style was chosen because it yielded the highest fired MOR values among the three different styles that were tried. The reason why this particular geometry was chosen was twofold. First, it would be relatively difficult to build through conventional forming techniques. But also, with its hollow interior, it would pose a challenge to the regular 3DP practice of isopressing ceramic green bodies prior to firing. The specifics of how the current process was modified to solve this problem is detailed in section 3.3.2.

Prechambers are used in diesel engines, as an alternative to two other existing fuel injection methods, namely direct injection and swirl chambers. The prechamber component is an important part of the combustion chamber, occupying about 20% of its total volume. Mercedes-Benz car Diesel engines use prechambers exclusively. This is because of the fuel economy and superior driving comfort that prechambers provide over the alternative injection methods [Gasthuber, 1988].

3.2.3 Silicon Nitride Bars

Rectangular bars (0.46x0.46x3.8 cm) were printed on the protomachine using the linear raster print style. Silicon nitride was chosen to demonstrate the adaptibility of 3DP to different ceramic powder systems. The binder was 6 vol% as in the case of fine alumina powder. The spreading mechanism was the press-rolling sequence suited for nongranulated, fine powders. The other printing parameters are tabulated in Table 3.1. The bars were used to determine the mechanical strength of 3DP-derived silicon nitride via 4-point bend testing.

3D-printed part	print style	layer height (μm)	line spacing (μm)	binder flow rate (cc/min)	fast axis speed (m/s)	binder saturation (%)
Alumina bars	linear raster	178	170	1.2	1.5	61.6
Alumina bars	staggered	125	225	0.89	1.5	49.1
Alumina bars	checker	100	202	0.89	1.5	47.1
Alumina prechambers	linear raster	120	200	0.89	1.5	57.5
Silicon nitride bars	linear raster	178	170	1.2	1.65	55.6

Table 3.1 The printing parameters used in making the parts referred to in this thesis.

3.3 Post Processing and Firing

3.3.1 Alumina Bars

Following printing, the bars were left to cure at room temperature. They were retrieved from the powder bed using soft brushes. Thin latex bags were used for

isopressing. The bars were placed in these bags, evacuated, and sealed before being placed in the oil chamber of the isopress. Isopressing was done at 40 ksi. Some samples were cold isostatically pressed (CIP) at room temperature while others were warm isostatically pressed (WIP) at 80°C. Dimensions of bars were measured before and after CIP/WIP. Following binder removal at 450°C for 3 hours, all bars were heated at 10°C/min to 1650°C in air, held at temperature for 2 hours, then allowed to cool.

3.3.2 Alumina Prechambers

These complex parts with their hollow interiors could not be isopressed directly like the bars. They had to be completely imbedded in (or at least filled up on the inside with) some sort of support medium. Three different powders were tried as support medium. In the first trial, the part was completely surrounded with spray dried alumina containing 2 wt% PEG (M_w = 4,600). The high flowability of the spray dried granules ensured uniform packing of the powder inside the powder. This is necessary for preventing distortion during shrinkage. The part was WIPed inside a latex bag at 80°C and 40 ksi pressure. The part retrieval strategy was to exploit the difference in dissolution characteristics of the polyacrylic acid (PAA) binder present within the part and the polyethylene glycol (PEG) present within the surround powder. The PAA, by itself soluble in water, becomes insoluble when chemisorbed onto the alumina particle surfaces. PEG, on the other hand, does not chemisorb and has a high solubility in water even at cold temperatures.

The part was removed from the bag and ultrasonicated in acidic water (pH = 3) at 70°C. The water was heated above the melting temperature of the PEG (~60°C) and the pH kept low to facilitate the redispersion of the alumina particles. As the PEG expanded upon melting, the compacted powder on the outside of the part, cracked and separated from the part easily. The powder on the inside, on the other hand, constrained by the part, depended solely on dissolution and redispersion. In order to facilitate the transport of water, thin drill heads were used to drill holes in the powder compact. Alternatively, 2 mm diameter metal wires were placed in the powder inside the part prior to isopressing. The wires were then pulled out after isopressing leaving channels for water access. These strategies were also tried in combination with a higher PEG content alumina (10 wt%) as surround powder. The rate of dissolution in all cases was too slow to be of any practical use.

Finally, pure PEG powder (M_w = 8000) was tried. The powder was compacted inside the part (47 % PEG, 53% porosity) by gently tapping with a flat spatula. The part was not surrounded with powder on the outside. Isopressing was done at 40 ksi, and room temperature. The part was placed in cold distilled water. To facilitate dissolution of the PEG, the water was stirred using a magnetic stirrer. Enough of the PEG had dissolved away within 1 h so that the remaining portion could simply be pulled out. The part was then rinsed in hot water and dried.

The prechamber part was then placed in an alumina crucible and surrounded by zircon grog. No grog was put inside the part because the zircon grog itself was found to

start sintering at the firing temperatures. The debinding and firing schedules were the same as the one used for the bars (section 3.3.1).

3.3.3 Silicon Nitride Bars

All silicon nitride bars were WIPed at 40 ksi and 80°C prior to binder burnout at 450°C for 3 h. They were then placed in a boron nitride coated graphite crucible and imbedded in H.C. Starck silicon nitride powder (grade T). The firing was done in a Centorr furnace (Materials Research Furnaces Inc., Suncook, NH) under N_2 atmosphere at 2 psi above atmospheric pressure. Parts were heated at 10°C/min to 1775°C, held at temperature for 3 h, and cooled down to room temperature at 30°C/min.

3.4 Mechanical Testing-- Four Point Bend Testing

Alumina bars were tested in the as-printed green state as well as the fired state. The green bars were broken on the 4-pt bend apparatus built by Charnnarong. Stainless steel powder was poured at about 3 g/s into a beaker attached to the top plate of the apparatus until the bar was broken. The load that broke the bar was weighed by a Mettler Electronic Balance.

The fired alumina and silicon nitride bars were ground down to standard size (i.e. width = 2.0 mm, depth = 1.5 mm, and length = 25 mm) and the edges chamfered (to minimize machining damage) by Bomas Machine Specialties Inc., Somerville, MA. The bars were broken on the Instron and the maximum load recorded. A four-point bend fixture was used in breaking the bars. The support span was 20 mm; the loading span

was 10 mm. The crosshead speed was 0.2 mm/min. The specimen size and shape, and the testing procedures were in strict compliance with configuration A of ASTM standard C1161-90.

3.5 Microstructural Analysis

Fracture surfaces of the fired alumina bars were examined for defects using a Hitachi Scanning Electron Microscope with a beam energy of 20 kV. SEM was also used to look at the different surfaces of fractured green bar segments. However, optical microscopy of polished cross sections of partially sintered bars revealed a much clearer image of the green microstructure. A total of nine as-printed green bars were first fired directly (i.e., no WIP) in air at 1450°C for 2 h to give them enough green strength for the subsequent operations. These were fast, slow, and z bars printed using the three different print styles. The bars were mounted in epoxy and polished using diamond pastes down to 9 μm. The normals to the polished cross sections corresponded to the fast, slow, and z axes of the 3D-printer. The epoxy was poured in in two steps so that, initially, it would cover the bars only partially. The assembly was then kept under vacuum for 5 minutes to help with infiltration of the epoxy before the rest of the epoxy was poured in.

The bulk density of fired parts and the intergranular porosity within as-printed green bars were determined by mercury porosimetry using a Micromeritics Autopore II machine. Sample sizes were ~ 1 g in a penetrometer with ~ 3 cc volume.

CHAPTER 4

RESULTS AND DISCUSSION

4.1 Alumina Bars

4.1.1 Fired Bars

Mechanical Characterization

Testing procedure

The maximum tensile stress, or Modulus of Rupture (MOR) is obtained by modelling the test bar as a beam under two point load with simple supports and is given by the following equation:

$$\sigma_{max} = \frac{3Fl}{bh^2} \tag{4.1}$$

where σ_{max} = maximum stress

F = load at fracture

l = distance between load point and nearest support point

b = width of sample

h = thickness of sample

The stress values thus obtained were multiplied by a factor of 1.04 to correct for the effect of the chamfer-- the edges of specimens had been chamfered (in accordance with ASTM standard C1161-90) to minimize machining damage.

CIP vs. WIP

The fired strength results for CIPed and WIPed linear raster bars are plotted in Figure 4.1. First, WIP generally results in higher MOR values than CIP. This is due in part to the higher initial green density achieved by WIP, i.e. by performing the isopressing step above the T_g of Acrysol (46°C). WIPed bars shrink more than CIPed bars by as much as 2.9% of their original volume in the case of slow bars. The WIPed slow bar bulk density average was ~ 62.8 %. The bulk density average was ~ 59.0 % for CIPed slow bars. More porosity is eliminated during WIP as compared to CIP, leading to fewer and/or smaller critical flaws in the final product. Secondly, among all the bars, the difference in fired strength between WIP and CIP is most obvious in the case of z bars. This is due to the fact that defects exist predominantly between layers. Thus, they are the smallest in z bars, and have the best chance of getting "healed" during WIP. WIP has been preferred over CIP because of its effectiveness in producing parts with superior fired strengths. Mercury porosimetry did not show any significant difference between CIPed and WIPed bar fired densities; fired bulk densities ranged from 97 to 99% theoretical.

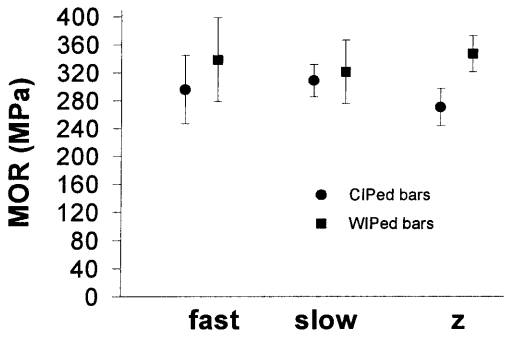

Figure 4.1 MOR values for fired linear raster bars
that were CIPed or WIPed prior to firing.

Contamination defects vs. 3DP-induced intragranular porosity

The strengths for all the fired alumina bars were plotted against print style in Figure 4.2 and against loading direction in Figure 4.3. The staggered style produced the highest strengths. The MOR values generally fell into the same range within each print style. One notable exception was the checker slow bars. These had considerably higher strengths than the checker z bars. This may be due to the fact that they were almost free of any visible contaminant particles. Checker fast and z bars, most of the linear raster bars, and especially the staggered bars contained a significant amount of contamination.

The contamination was visible as dark red spots on the surface of the bars. Optical microscopy revealed rough, porous regions, approximately 100 μm in diameter, made up of a shiny, metallic phase (Figure 4.4). These particles had evidently inhibited the densification process in these regions. The concentration of the metallic phase was too low to be detected by EDAX. These contamination-induced pores provided another

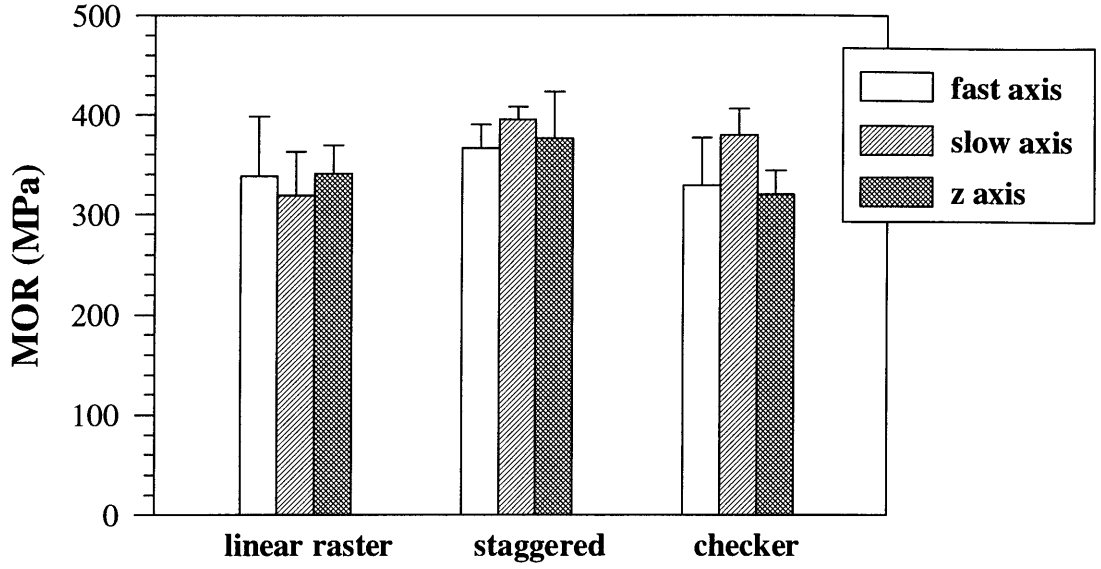

Figure 4.2 Mean fired strength vs. print style.

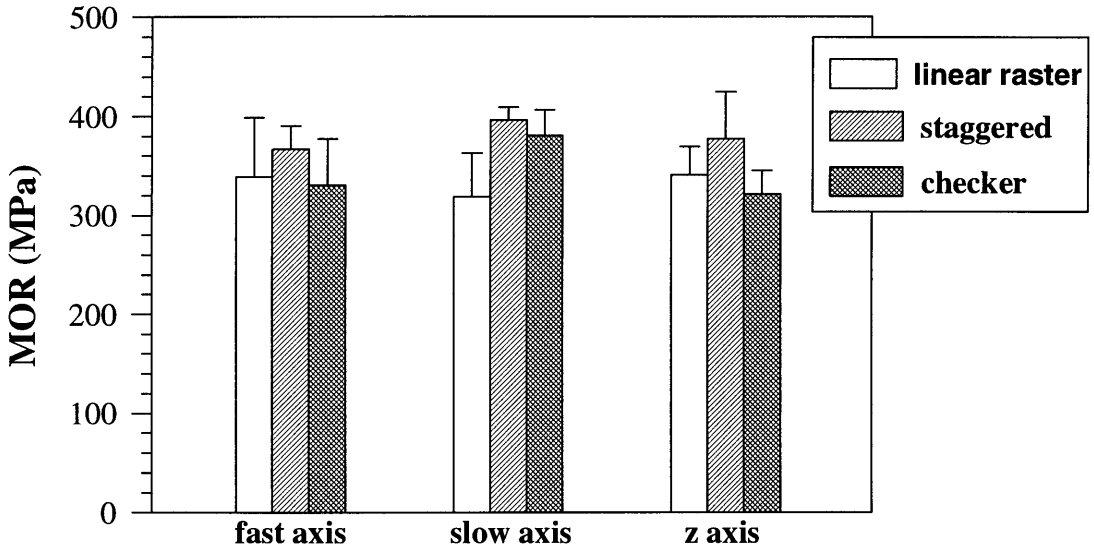

Figure 4.3 Mean fired strength vs. loading direction.
Staggered bars showed the highest strengths.

set of potential strength limiting flaws next to processing related intergranular porosity and surface defects due to grinding.

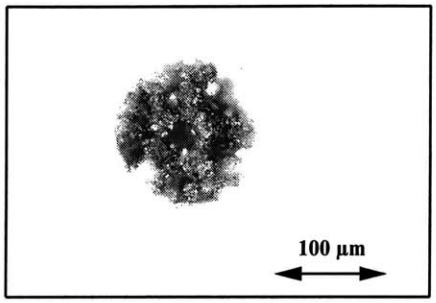

Figure 4.4 Optical micrograph of a metal contaminant particle on an alumina bar surface.

Direct evidence that these contamination-induced defects may indeed have been the cause for fracture in some cases came from examination of the broken pieces of alumina. The fragments were brought together, matching the two halves of a split contamination spot located on the tensile surface in 3 of the 15 checker z bars that were examined. Cross contamination from printing of stainless steel powders is suspected to be the source of these contaminant particles.

Each set of bars was examined for a correlation between fracture strength and number of contamination particles visible on the tensile surface, both parameters averaged over the whole set. Most of the staggered fast bars contained about 30 particles/cm^2, and had an average strength of 370 MPa. The few that contained 80 particles/cm^2 or more had strengths of about 240 MPa. The same trend was observed for the staggered slow bars, most of which contained 0-2 particles/cm^2, averaging 396 MPa in strength. The two bars that contained 50 and 56 particles/cm^2, had strengths of 291 and 245 MPa, respectively. Similarly, checker slow bars were free of contamination and

had significantly higher strengths than the contaminated checker fast and z bars (Figure 4.2).

Evidently, a correlation does exist among the fast, slow, and z staggered bars as well as the checker bars-- a higher concentration of contaminant particles generally leading to lower fracture strength. This suggests that, in staggered and checker bars, the strength limiting flaws are the contamination-induced pores. The implication is that, in these bars, the 3DP-induced intergranular pores measure less than the metal-induced defects on average, i.e. less than about 100 μm. This was confirmed by SEM analysis.

Linear raster bars were less heavily contaminated than staggered bars. Nevertheless, they had lower fired strengths (Figure 4.3), ruling out the possibility that the metal-induced pores were the strength limiting flaws in both cases. Indeed, no correlation between the number of contamination particles and strength was found in the case of linear raster bars. In fact, linear raster fast bars, with an average of 12 particles on their tensile surfaces, had a higher average strength than the slow bars, which contained almost none. This, along with the fact that the longest residual intergranular pores were observed in linear raster slow bars (~320 μm in Figure 4.6) among the entire set of 3D-printed bars suggests that the dominant cause for failure in linear raster bars was residual intergranular porosity.

Intergranular porosity in fired linear raster bars consisted of long (as much as 320 μm) narrow serpentine channels. The separation between the ~40 μm diameter spray dried granules that made up the walls of these channels was on the order of 4 μm. A quick calculation reveals that this separation can arise as a result of the difference in

relative green density between the lower-density uncollapsed granules (~50% theoretical) and the higher-density collapsed powder (~60%).

Microstructural Analysis

Fractographs of fired bars revealed long linear defects oriented along the fast and slow axes, clearly implicating the 3DP process. The defects appeared in the form of isolated regions of intergranular porosity between spray dried granules that the isopressing step had failed to collapse. Figure 4.5, a fractograph of a fired linear raster z bar shows such defects along the fast axis-- between lines. The cross section of a fired linear raster slow bar in Figure 4.6 shows lamination defects between layers. Figure 4.7 shows the same defect as Figure 4.6 at the top left-hand corner and another running parallel to it along the bottom. The two lines of defects are oriented along the fast axis; they lie 270 μm, i.e. roughly two layers, apart. Defects in the case of fired linear raster fast bars were found in seemingly random locations.

A control experiment in compaction

Kamiya et al (1995) have found that intergranular porosity is a strong function of the fracture strength of individual spray dried granules. Depending on the amount of binder present within the granules, stresses of up to 800 MPa may be required to completely collapse intergranular porosity. Thus, the control experiment described in section 3.2.1 was done to confirm that 240 MPa, the isostatic pressure used in our experiments, was high enough to completely collapse the granules. The experiment was

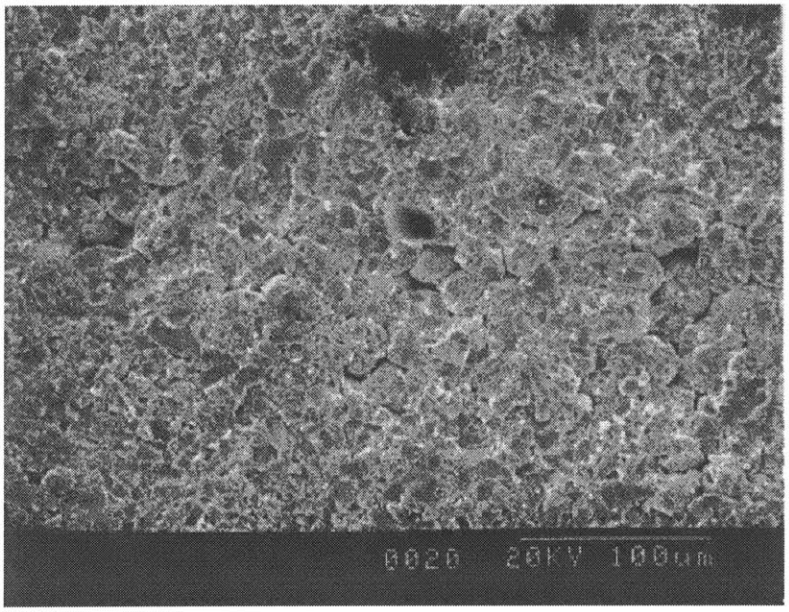

Figure 4.5 Fractograph of fired linear raster z bar showing intragranular pores between lines.

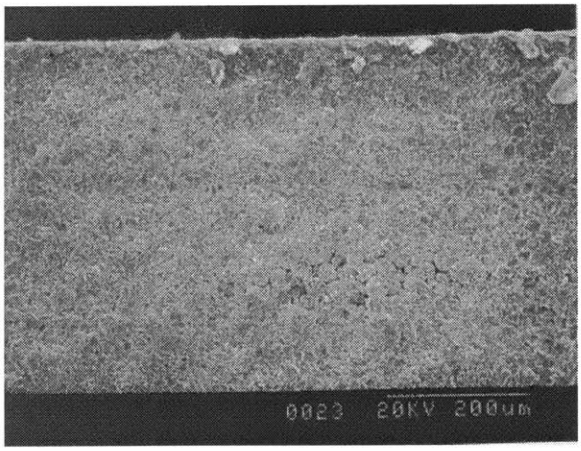

Figure 4.6 Fractograph of fired linear raster slow bar, showing a ~320 μm lamination defect.

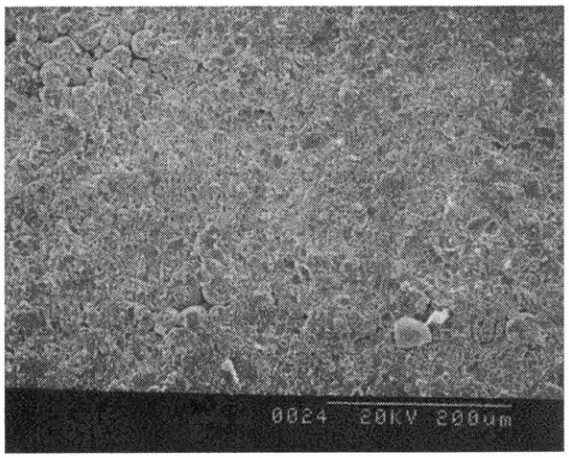

Figure 4.7 The same defect in Fig. 4.6 at the top left-hand corner & another defect parallel to it 270 μm (~ 2 layers) below.

done on the larger size spray dried powder (average granule size ~45 μm) used in fabricating the checker bars. Fracture surfaces of the loose spray dried powder WIPed and fired in the same way as the printed bars did not show a single intergranular defect. This result proved that the granule strength, at least for this particular batch of spray dried powder, was sufficiently low for complete collapse under 240 MPa. Thus, the defects observed in fired checker bar fractographs could only be due to the 3DP process.

Linear raster bars vs. staggered and checker bars

Fractographs revealed fewer and smaller intergranular defects in staggered and checker bars compared to linear raster bars. Polished cross sections of fired staggered and linear raster bars provide a comparison between the two print styles. Figures 4.8-4.13 show that the defects observed between lines and layers in linear raster bars are largely absent in the case of staggered bars. The improved microstructure could be a print style related effect. However, it could also be attributed to the lower printed binder content or to the larger size spray dried granules. A lower binder content would have reduced the number of cases where excess binder between granules prevented them from merging together during isopressing. The granule size effect is described below.

According to Kamiya et al, while granule strength is independent of granule size, the mean force at contact points between granules varies as the square of the mean granule size. The granules used in fabricating the staggered and checker bars were on average 1.6 and 1.3 times larger than those used for the linear raster printing run, respectively. Thus, the contact force felt by these larger granules would have been

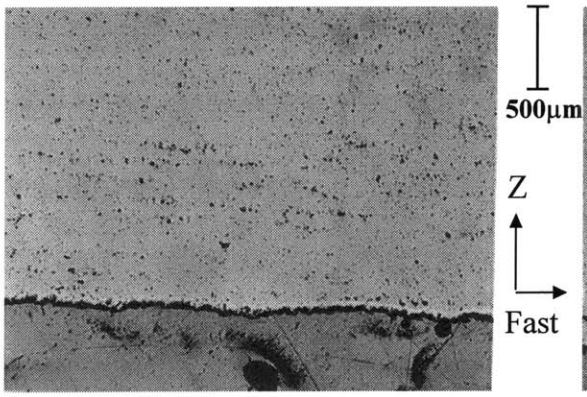

Figure 4.8 Fired linear raster bar cross section showing lamination defects.

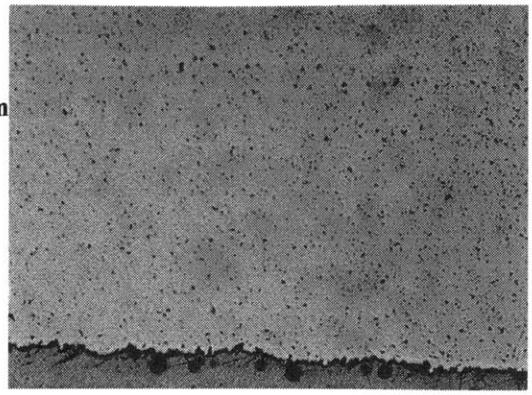

Figure 4.9 Fired staggered bar cross section. No lamination defects are present.

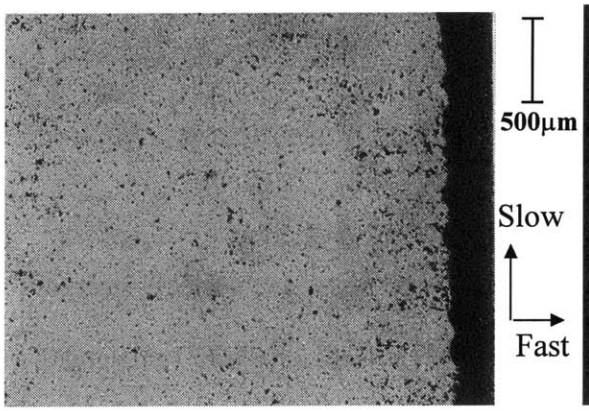

Figure 4.10 Fired linear raster bar cross section showing defects between lines.

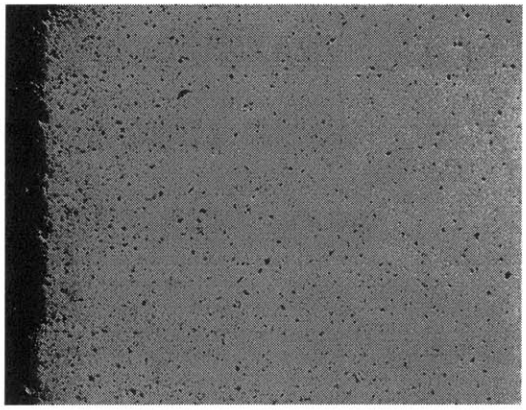

Figure 4.11 Fired staggered bar cross section. 3DP-related defects are absent.

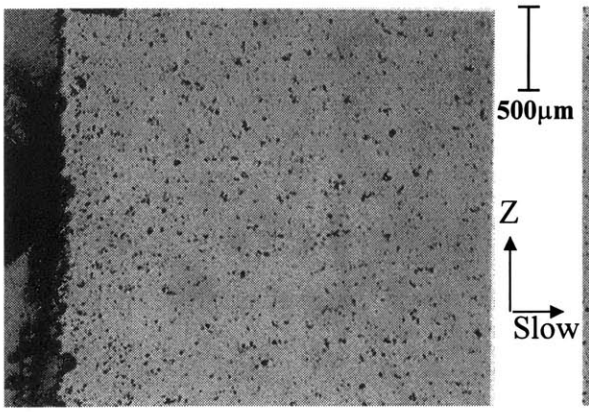

Figure 4.12 Fired linear raster bar cross section showing large pores between layers.

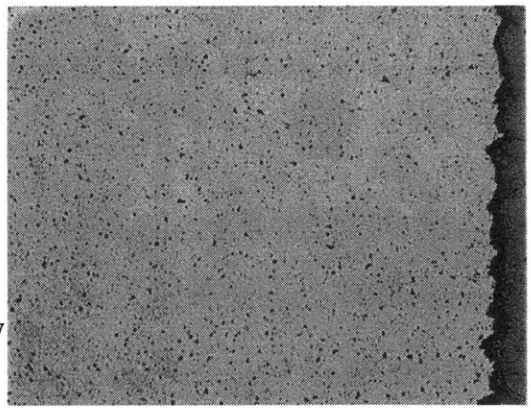

Figure 4.13 Fired staggered bar cross section. Porosity is much finer.

roughly 2.5 and 1.7 times higher, leading to a higher proportion of collapsed granules in the case of the staggered and checker bars-- one possible explanation for the observed microstructural differences.

4.1.2 Green Bars

Mechanical Characterization

The MOR values were calculated using Equation 4.1. Each type of bar was loaded in two different directions (Figure 3.4), creating a total of six distinct tensile stress conditions along two orthogonal axes in three orthogonal planes as shown in Figure 3.5.

MOR standardization calculations

Staggered and checker bars were printed with 20% less Acrysol solution than linear raster bars. This may have caused a decrease in green strength not only by reducing the binder at the necks between granules, but also by affecting the rearrangement behaviour of the powder. However, the powder in the case of staggered and checker bars also consisted of larger spray dried granules which reduces the total surface area per gram of powder available for soaking up printed binder. The net effect of these changes in the amount of printed binder and granule size was estimated by measuring the average radii of granules and of binder necks formed between granules for the three different printing runs. Multiplicative factors were determined using these measured quantities for the staggered and checker bars so that they could be put in fair comparison with the linear

raster bars. The underlying assumption in these calculations was that the differences in average binder neck size between the three print styles was attributable solely to the differences in granule size and binder content. This presupposes the inter- and intragranular porosity to be similar in the three cases, which was verified by mercury porosimetry (Table 4.1).

Fractographs of green bars revealed most of the intergranular Acrysol binder to be located at the neck regions between spray dried granules rather than forming a continuous coating. Onoda (1976) refers to this as the pendular state. He derives the following equation for $S_{pendular}$, the strength of a green body held together by pendular bonds, based on Rumpf's equation for the tensile strength of a body consisting of randomly packed spheres of uniform diameter:

$$S_{pendular} = \frac{3\pi\sqrt{3}}{8}\frac{(1-p)}{\sqrt{p}}\left(\frac{V_b}{V_p}\right)^{1/2} S_o \tag{4.2}$$

where p = volume fraction of intergranular pores

V_b = total volume of binder located at necks

V_p = total bulk volume of all spray dried granules

S_o = strength of an individual pendular bond

But the cross sectional area A of the pendular bonds is given by

$$A = \pi r^2 = \frac{4\pi R^2}{(3k)^{1/2}}\left(\frac{V_b}{V_p}\right)^{1/2} \tag{4.3}$$

where r = binder neck radius,

R = spray dried granule radius,

k = average number of touching neighbor granules,

and V_b, V_p are as previously defined. Eliminating $(V_b/V_p)^{1/2}$ between Equations 4.2 and 4.3, and using the mathematical relation $k = \pi/p$ derived by Rumpf, we get:

$$S_{pendular} = \frac{9\pi^{3/2}}{32}\left(\frac{1-p}{p}\right)\frac{r^2}{R^2}\,S_o \tag{4.4}$$

The p values were measured by mercury porosimetry. For R and r, average values were used. For each print style, the R_{ave} and r_{ave} were determined by averaging 10-15 values measured on SEM photographs. The r values were found to increase with R according to some weaker-than-linear relationship. The volume fraction of intergranular porosity (p), the bulk density of the printed bars and of the spray dried granules making them up, and the minimum, maximum, and average values for R and r are given in Table 4.1.

Print style	p (%)	Bulk ρ of granules (% theoretical)	R_{max} (μm)	R_{min} (μm)	R_{ave} (μm)	r_{max} (μm)	r_{min} (μm)	r_{ave} (μm)
linear raster	40.0	47.5	30	8	18	7.1	5.4	6.7
staggered	42.8	50.0	43	12	28	11.4	5.8	8.6
checker	42.6	49.5	35	15	23	9.0	7.2	8.0

Table 4.1 Comparison of the three print styles with respect to intergranular porosity, granular bulk density, radii of the spray-dried granules, and the radii of the necks between them.

The constants for factoring out the combined effect of having a lower binder content and a lower total surface area with compared to the linear raster bars on the green

strength of staggered and checker bars were calculated using Equation 4.4 to be 1.60 and 1.27 for the two print styles, respectively. The raw MOR values for staggered and checker bars were multiplied by these constants before they were plotted alongside the linear raster bar green MORs in Figures 4.14-4.16.

MOR as a function of loading direction-- anisotropic internal defects

The linear raster MORs and the staggered and checker modified MORs are plotted against print style in Figure 4.14. The MORs associated with loading directions 1 through 6 form the same general outline in each of the three print styles. Loading the same type of bar in different directions sheds light on the interior structure of the green bar. Figure 4.14 shows that loading fast and slow bars in the z axis generally yields lower MORs than loading these bars in the slow and fast axes, respectively. This result is expected if defects occur predominantly *between* layers, i.e., if defects have larger cross sections in the fast-slow plane. Loading direction 1 and 3 in Figure 3.4 will then create a tensile plane that will cut across the *larger* cross sections of these defects, resulting in *lower* MOR values compared to loading directions 2 and 4. In the case of z bars, loading in the fast and slow axes (directions 5 and 6) yields almost identical mean MOR values since, this time, the tensile plane for both loading directions "sees" only the *thin* cross section of the defects.

Loading bars in directions 1 and 2 measures stitching along the fast axis, 3 and 4 along the slow axis, and 5 and 6 along the z axis. Figure 4.15, obtained by averaging the MORs for the two directions in each of these pairs, shows a trend of decreasing MOR as

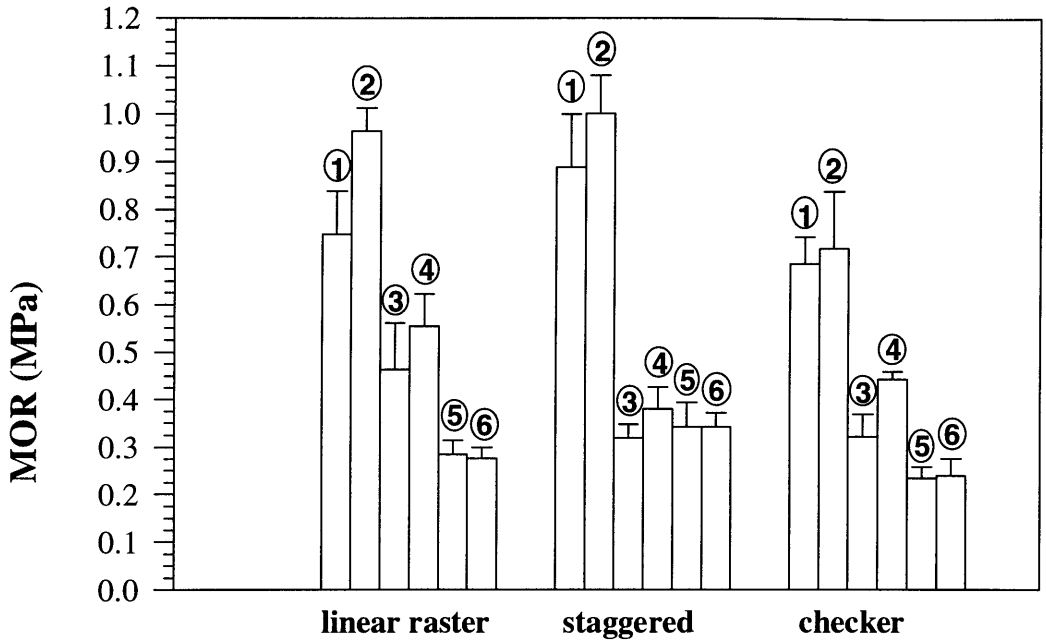

Figure 4.14 Standardized green MORs vs. print style. The numbers 1-6 represent the different loading directions (see Figures 3.4 & 3.5).

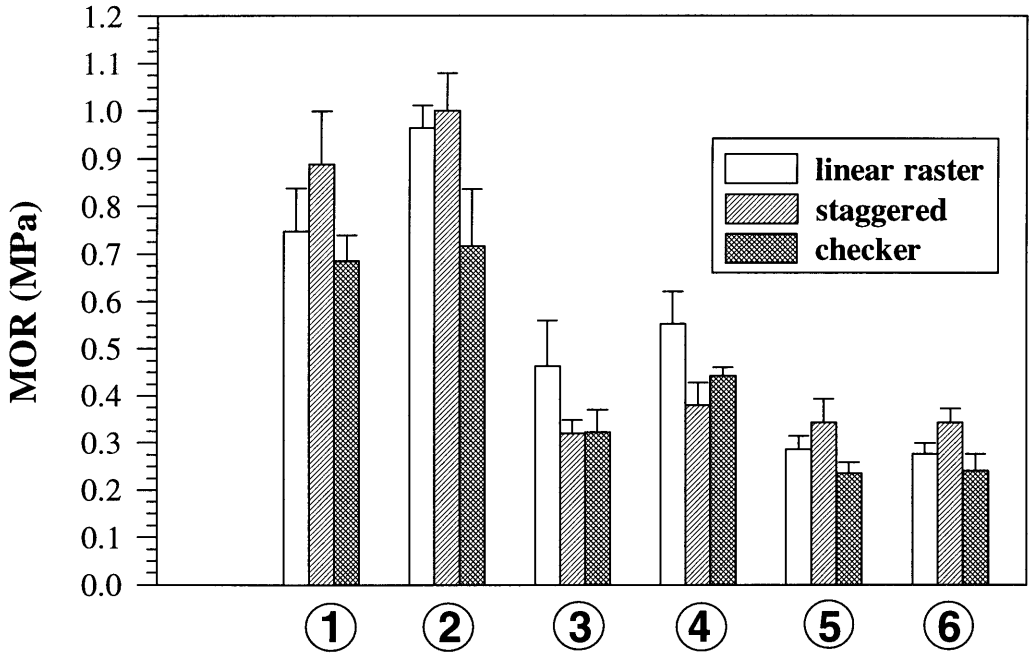

Figure 4.16 Standardized green MORs vs. loading direction

one goes from fast to slow to z bars for each print style. The normalized average MOR ratios are indicated below the x axis. Green strength anisotropy is lowest in the case of staggered bars. The MOR ratio of fast to z bars drops from 3.0 (in linear raster bars) to 2.8, and the MOR ratio of slow to z bars from 1.8 to 1.0. The reduced layer height and the staggering of lines are sure to have played a role in this.

Effects of printing parameters/style on MOR

Figure 4.16 plots the same green strength data as a function of loading direction for a comparison between the three printing runs. The staggered style is observed to improve stitching along the fast and z directions. The strength along the z direction is presumably increased as a result of the reduced layer height and the close packing of lines. Checker bars show higher strengths along the slow axis than staggered bars. This is due to the greater line overlap achieved between lines through proportional deflection.

MOR as a function of surface characteristics

The printhead in the alpha-machine rasters the powder bed starting from the back so that the back surfaces of parts are composed of the first printed line in each layer. The printed lines that constitute the back surfaces of both fast and z linear raster bars are observed to be straighter and less prone to flaking during unprinted powder removal than those making up the front surfaces. This may be due to differences in binder migration in the two cases. The wetting characteristics presumably dictate that while the first line of binder wick freely in all directions, the last line of binder migrate preferentially towards

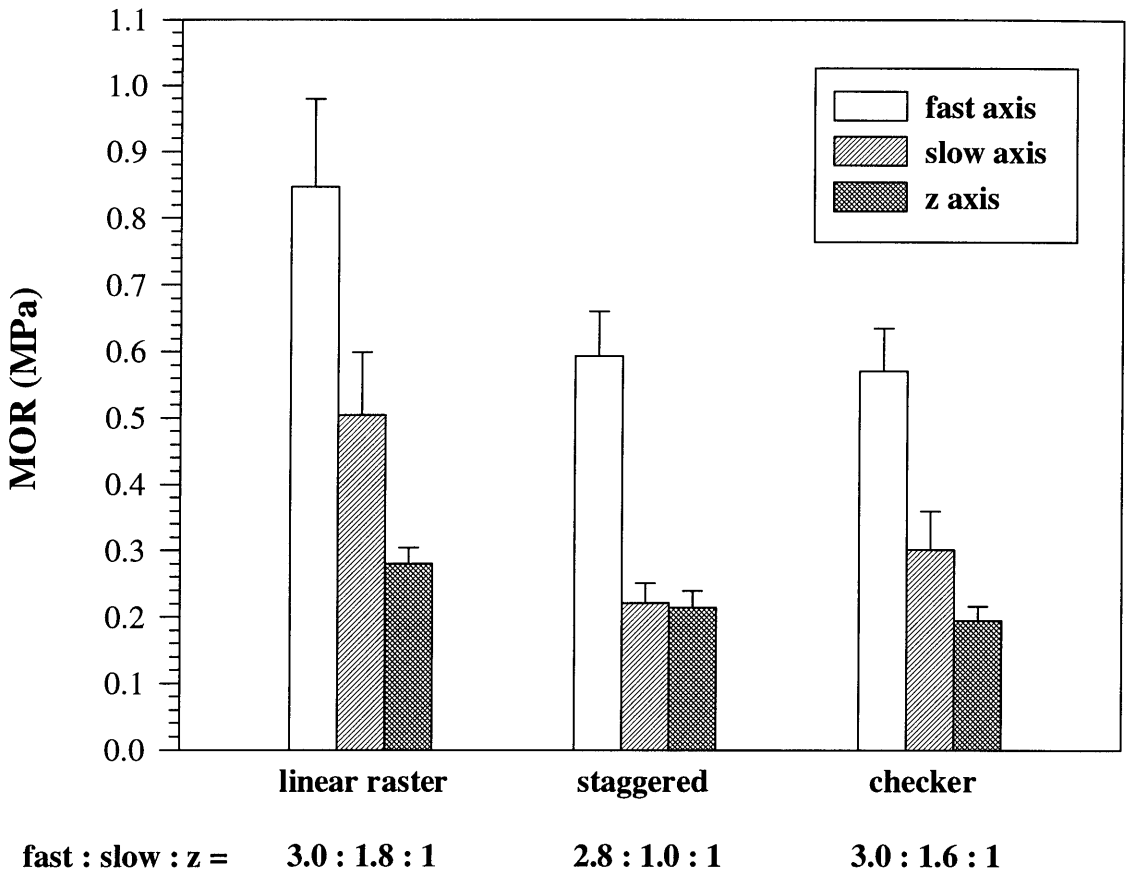

Figure 4.15 Standardized green MORs vs. print style. Average MOR ratios along the fast, slow, and z axes are given for the three print styles.

the printed region. Four-point bending with back surfaces in tension yields slightly higher MORs than with front surfaces in tension. This is because the larger surface defects on the front surfaces are more effective as crack initiation sites. Tensile loading of top vs. bottom also yields different strengths in linear raster bars tested under 4-pt. bending. The effects of surface characteristics were not investigated for staggered or checker green bars.

Microstructural Analysis

Lines--Isolated single, double, and quadruple line sequences, and lines in multilayered parts

Spray dried powder beds are prone to a tremendous amount of ballistic ejection by virtue of their low cohesive strength. Fig 4.17 is a stereomicrograph of a *single printed line* as viewed from above. The two dark regions on either side of the line are the edges of a plateau at the bottom of a deep crater formed by the ballistic interaction between the binder droplets and the powder bed. Fig 4.18 (a) is a schematic of the side view of a single line. Typical dimensions that were observed are provided in Figure 4.18 (b).

The line sits at the bottom of the crater with a clearing on either side between it and the crater walls. The binder droplets printed on a virgin powder bed evidently travel a relatively long distance (~ 500-800 μm) before they lose their momentum and come to rest. The spray dried granules are then pulled together as a result of binder surface tension forces, forming a cylindrical line. The net shrinkage which accompanies this rearrangement process and the subsequent drying results in the formation of the gaps

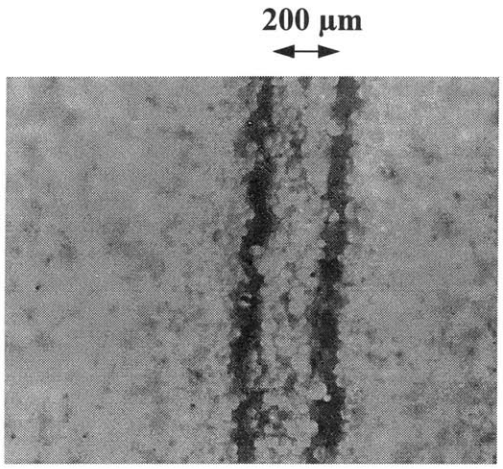

Figure 4.17 Stereomicrograph of an as-printed single line (acrysol on spray dried alumina powder bed).

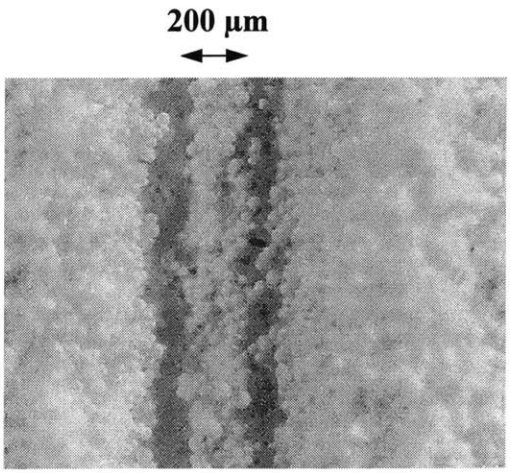

Figure 4.19 Stereomicrograph of two adjacent lines printed 178 μm apart. 2nd line forms to the left of 1st line, deeper in the powder bed.

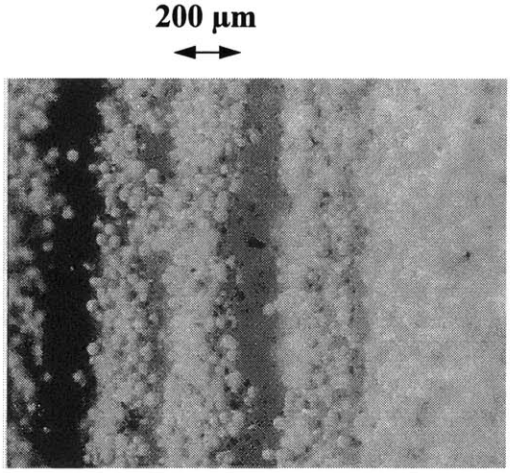

Figure 4.20 Stereomicrograph of four adjacent lines printed 229 μm apart. The 2nd line is again "missing." No merging btw. 3rd and 4th lines.

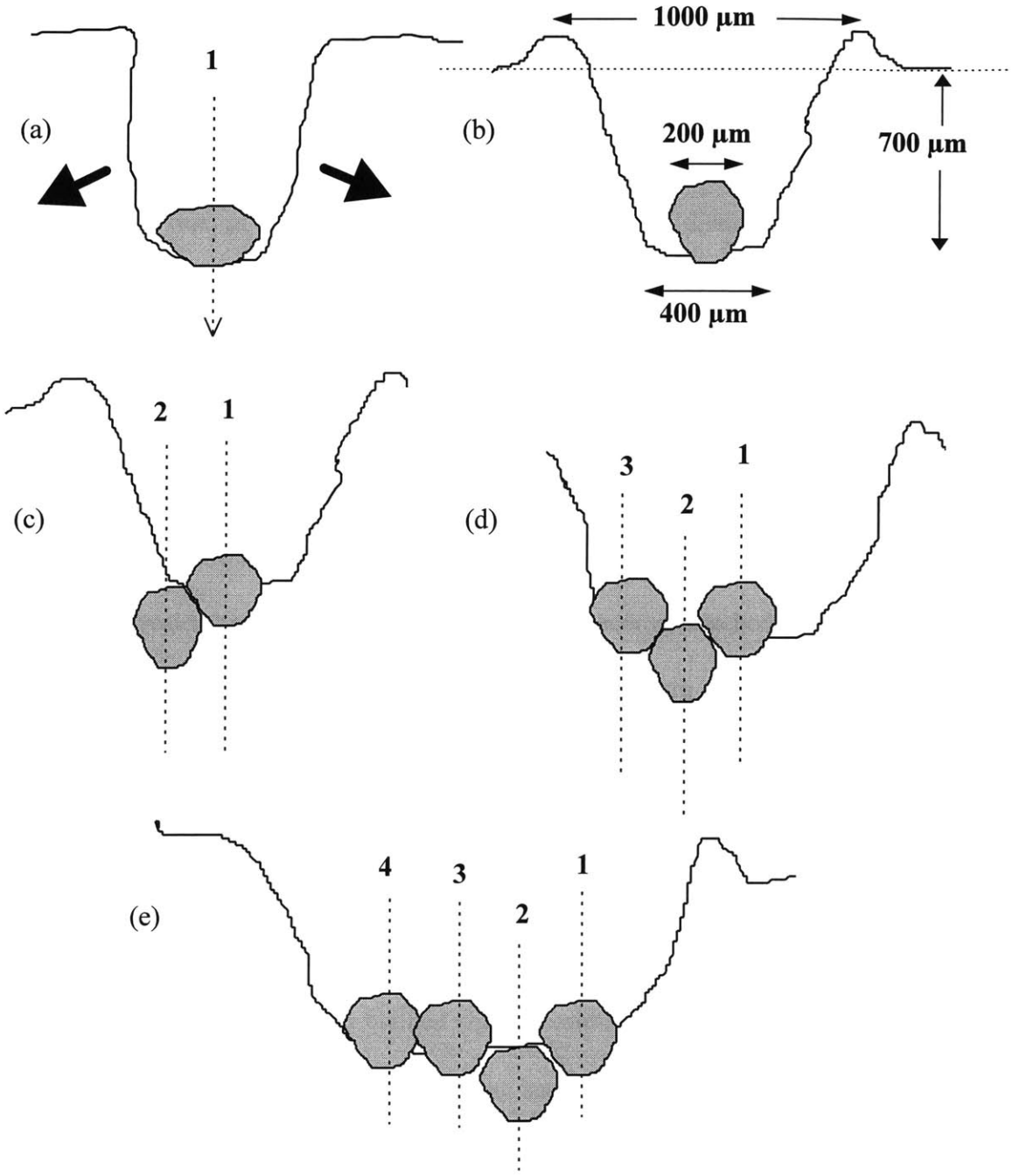

Figure 4.18 The ballistic powder\binder interaction creates a deep crater (a). Surface tension causes particles to rearrange and to form a cylindrical line (b). The walls of the crater recoil from the impact and fan outward. The next line printed 178 µm away (c) hits the powder bed at a lower level and is thus formed deeper in the powder bed than the 1st line. The 3rd (d) and 4th (e) lines hit steep crater walls so they form at about the same level as the 1st line.

observed on either side of the line (Figure 4.17). Each gap is roughly half a line diameter wide. The two crater walls diverge from each other at an (acute) angle. This is a result of the recoil from the ballistic impact (Figure 4.18 (b)).

A *double line sequence* is shown in Fig 4.19. The second line was printed to the left of the first line, at a 178 μm spacing in this case. A distinct second line is not observed in Figure 4.19. The possibility that the two lines had merged can be excluded by observing that the diameter is roughly the same as that of the single line shown in Figure 4.17. A closer examination of Figure 4.17 reveals that the second line would get deposited over the gap found on the left side of the first line. Indeed, lifting the line out of the powder bed from one end revealed the "missing" second line. It had penetrated deeper into powder bed than the first line and had become attached to it as shown in Figure 4.18 (c). The gap on the left side of the line in Figure 4.19 appears to be wider than the gap on the right side. This is possibly due to the fact that the second printed line has knocked off some of the granules on the crater wall. Similar observations were made for the double lines separated by 203 μm and those separated by 229 μm. However, the two lines were found to be unattached in the latter case due to the larger separation.

Quadruple line sequences yielded similar results for all three line spacings. The last two lines were both formed at roughly the same z level as the first line in all three cases. The fourth line was slightly elevated with respect to the first and the third lines in the case of the 203 μm separation sequence. Figure 4.20 shows the four adjacent lines (line spacing 229 μm) with the second line "missing." These lines are not expected to stitch well, if at all, to the lines in the next layer since they have buried themselves too

deep in the powder bed. This situation would continue until a moist, impact-resistant foundation has formed. The droplets would have at most only a layer height of dry powder to penetrate and ballistically interact with once this "steady state" is reached. Therefore, craters formed beyond the first few layers are expected to be shallower and narrower. The newly spread layer directly above the printed region generally gains in cohesive strength as it soaks up moisture from the previous layer. This would further reduce the width of the crater by reducing the impact recoil in the "steady state" region in *multilayered parts*. Lines would then have a better chance of merging since they would be forming at the about the same z level. Indeed, merged lines were observed only in the case of multilayered parts and not isolated line sequences.

The top surface of a WIPed fast linear raster bar (bulk density density ~60% theoretical) consists of an alternating pattern of merged and missing lines (Figure 4.21). The "missing" lines in this case are truly missing, i.e. they are not simply buried deeper in the powder bed. Rather, the binder gets "wasted" on a preexisting line in the previous layer exposed by the ballistic impact and is not used in forming a new line.

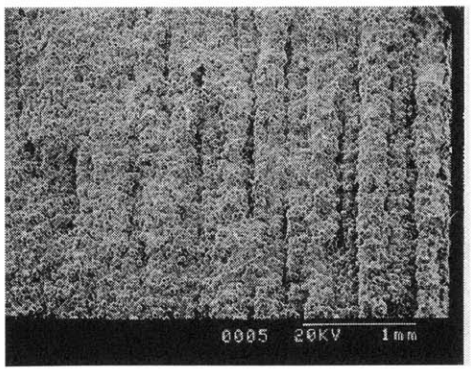

Figure 4.21 The top surface of a WIPed fast linear raster showing missing and merged lines.

One can imagine how the topology observed in Figure 4.21 would propagate once it has been formed. A given line would penetrate until it made contact with the previously printed line directly below it. The jagged profile in the slow-z plane would then be preserved until the top layer. Some of the grooves in Fig 4.21 are as wide as the merged line diameter (~ 315 μm). Adjacent lines printed over such a groove would be topologically confined to this region and thus most likely be forced to fuse together. The shrinkage associated with merging and subsequent drying would cause gaps to develop on either side of the merged line. This provides an important clue as to the mechanism of defect formation observed in polished cross sections of linear raster bars (Figure 4.27).

The nature of the interactions between individual lines is expected to be very sensitive to small variations in packing density and printing conditions (flow rate, placement of droplets) in addition to the topology, line spacing, and layer height. A small change in any one of these variables can be imagined to have a cascading effect on microstructure on a local level. Therefore, in general, the best way to ensure reproducibility might be to print lines as far apart as possible within each layer. The interaction between lines within a layer would then be minimized or even eliminated.

SEM fractographs of green bars

SEM fractographs of linear raster bars provided the first direct evidence for defect anisotropy within 3D-printed green bars, accounting for the observed strength anisotropy. The laminated nature of green bars was most obvious in linear raster green slow bar

fractographs like the one shown in Figure 4.22. The length scale of the distinct pattern does in fact correspond to the 178 μm layers. The layers are harder to see in the linear raster green fast bar fractograph shown in Figure 4.23. The rather random appearance indicates that, in contrast to the green slow bar fractographs, there is less of a continuous weak plane along which most of the printed lines were severed. This suggests that stitching along the fast axis, i.e. *within* a line, is stronger than along the slow axis, i.e. *between* lines.

Figure 4.24 is a linear raster green z bar fractograph showing the individual lines that make up a layer. The presence of the linear pattern is indicative of the fact that stitching along the fast axis is stronger than along the z axis. Further corroboration for this notion comes from shrinkage anisotropy measurements (Section 4.1.3).

Polished cross sections of partially sintered bars

Optical micrographs of polished cross sections of partially sintered bars capture the microstructural features of 3D printed (partially) green parts even more effectively than SEM fractographs. The dark spots seen in Figures 4.25-4.30 are pullouts that are created during polishing due to incomplete infiltration of epoxy. Bars undergo 10% linear shrinkage upon partial sintering. However, the defect structure is retained during shrinkage since shrinkage occurs largely as a result of *intra*granular sintering (neck growth between granules is minimal).

The lamination defects observed in the fast-z plane in the case of linear raster bars (Figure 4.25) are absent in staggered bars (Figure 4.26). This is a result of the reduced

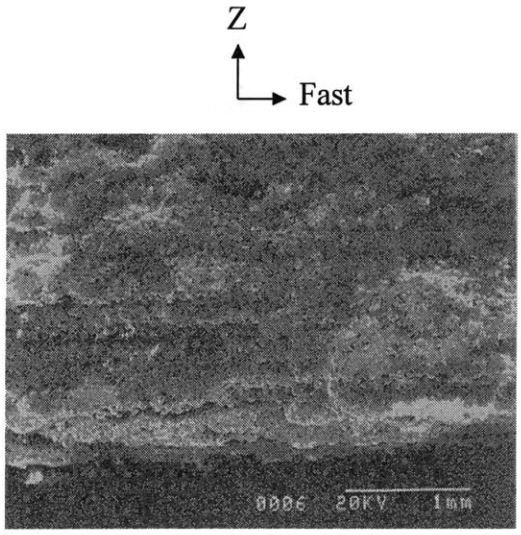

Figure 4.22 Fractograph of linear raster green slow bar showing layers.

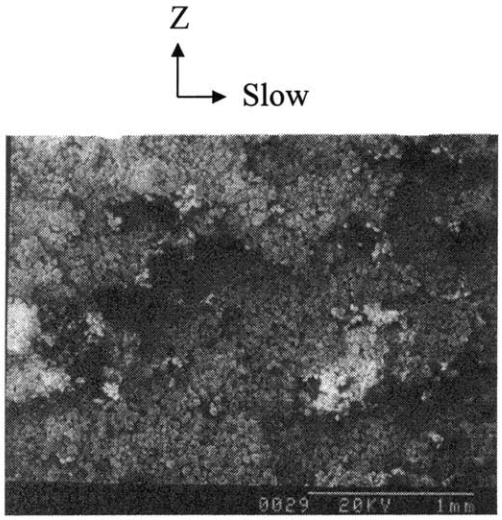

Figure 4.23 Fractograph of linear raster green fast bar.

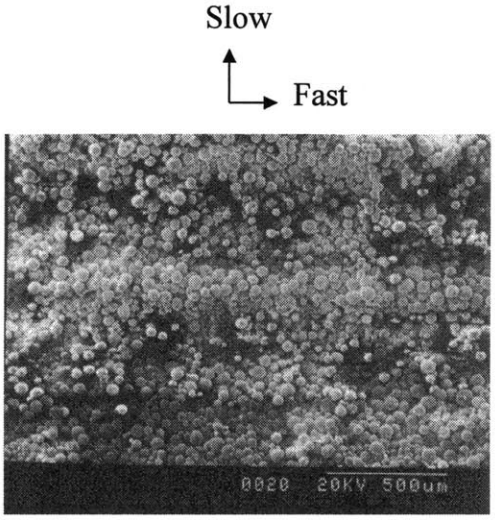

Figure 4.24 Fractograph of linear raster green z bar, showing lines.

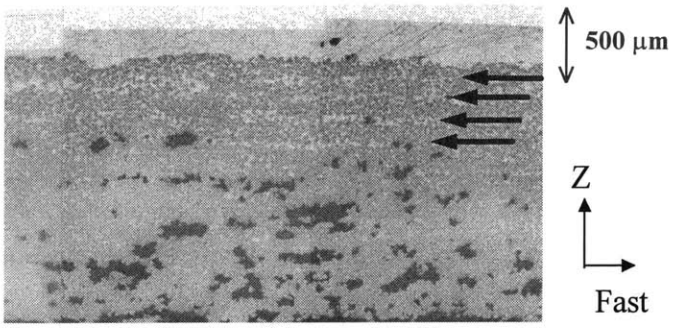

Figure 4.25 Defects between consecutive layers are indicated by arrows in this green linear raster fast bar optical micrograph.

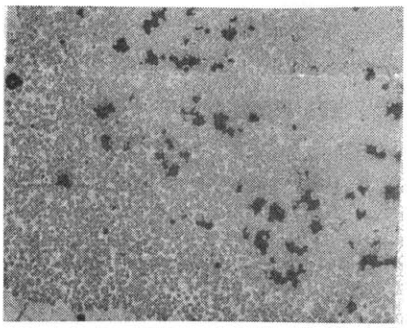

Figure 4.26 No defects between layers in the case of a staggered fast bar.

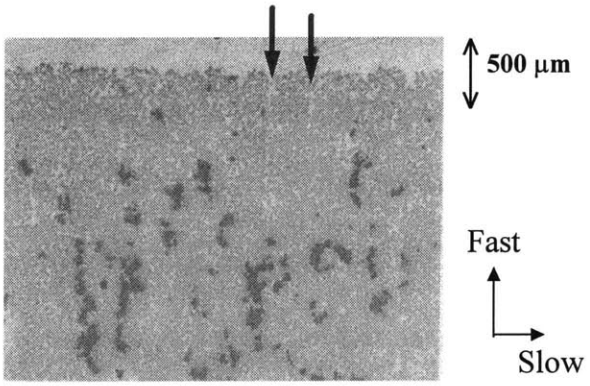

Figure 4.27 Defects between pairs of lines are indicated by arrows in this green linear raster fast-slow plane.

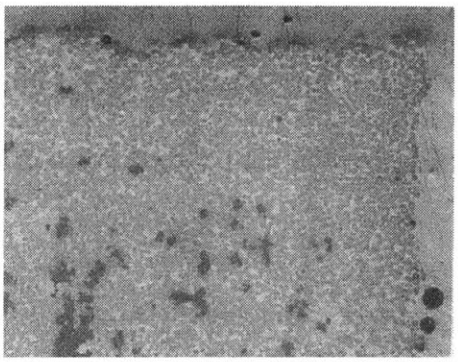

Figure 4.28 No defects between lines can be seen in the staggered fast-slow plane.

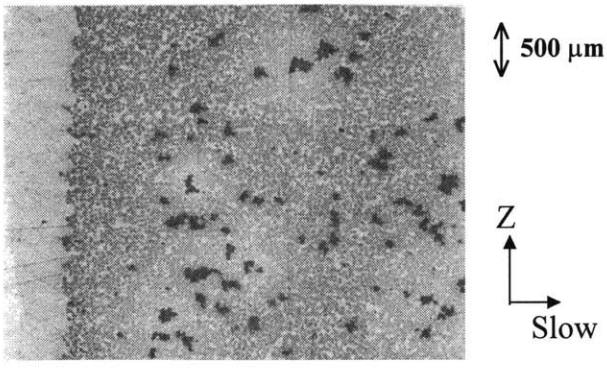

Figure 4.29 No clear patterns are obvious in this linear raster z-slow plane.

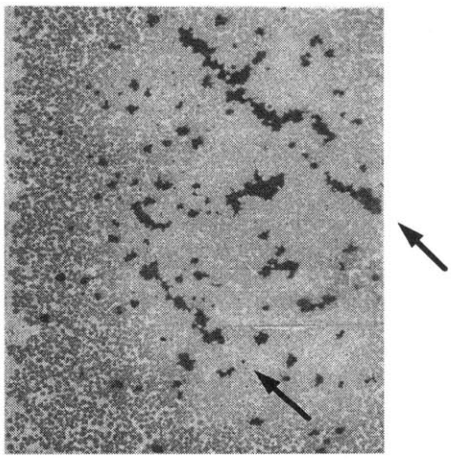

Figure 4.30 The two diagonal pullout lines are an effect of the line stagger used in the staggered style.

layer height and staggered line arrangement used in the staggered style. However, it can also be argued that the interlaminar defects observed in the case of linear raster bars were due to excess binder deposited between layers and that the 20% decrease in binder saturation alone helped avoid this.

Line merging effects [Lauder, 1992] are evident in the fast-slow plane in linear raster bars (Figure 4.27). A possible explanation of how these defects might have arisen has already been presented at the end of the subsection entitled "Lines--Isolated single, double, and quadruple line sequences, and lines in multilayered parts." No observable voids between lines are present in the case of staggered bars (Figure 4.28). Rather than print style differences, this observation can be arguably ascribed to differences in powder rearrangement behaviour caused by the 20% decrease in binder saturation. In other words, one might argue that line merging could still have been avoided in these bars if they had been printed at 20% lower saturation using the *linear raster style*. The reduced saturation alone may have been sufficient to push the system below the critical amount of binder necessary for complete line merging to occur.

A microstructural feature is observed in a staggered z bar cross section that is unmistakably an effect of the staggered print style. The spray dried granules in the slow-z plane are found to be arranged randomly with no interlaminar defects in either linear raster and staggered bars. The staggered bar pullouts, on the other hand, form a pattern that is clearly an effect of staggering lines in alternate layers. Pullouts are generally believed to highlight the defects that existed in the printed part since large defects, or voids, cannot exert the capillary pressure needed for complete infiltration of epoxy. The

two parallel pullout lines are inclined at a 45° angle between the slow and z axes in Figure 4.23. This corresponds closely to 42°, the calculated value obtained from the line width and layer height. No such pattern is observed in the slow-z plane in linear raster bars (Figure 4.30). In none of the three cross sections of checker bars was there any discernible pattern to be seen. Spray dried granules had rearranged to give a competely random, defect free microstructure as a result of the particular print style that was used.

4.1.3 Isopressing Shrinkage Measurements

Shrinkages along the fast, slow, and z axes were determined by measuring the dimensions of rectangular bars before and after the isopressing step. Shrinkage was found to be anisotropic. The least amount of shrinkage was observed along the fast axis, in good agreement with the high green strengths observed along this axis as compared to the slow and z axes. Shrinkage was also found to vary with print style.

Fine Powder

The first WIP shrinkage measurements associated with parts printed using the linear raster style were done for alumina bars [Yoo, 1993] fabricated via press-rolling of submicron size fine alumina powder. Shrinkage along the three axes was found to increase with temperature during isopressing (CIP vs. WIP), and the amount of printed binder (6 vol% vs. 12 vol%) [Yoo, 1993].

Spray Dried Powder

The majority of printing runs for this thesis were done using spray dried granules. The binder-powder interaction, and thus powder rearrangement behaviour is expectedly different in the case of the less cohesive powder beds made up of semihollow (~50% intragranular porosity) spray dried granules. The first shrinkage measurements for spray dried powders were done on bars printed with spray dried silicon metal powder and 6 vol% binder solution. The binder in this case was a mixture of 4.5 vol% Acrysol and 1.5 vol% PEG (M_w = 1000). The PEG was used as a plasticizer to prevent warpage during printing. Shrinkages were also measured for spray dried alumina bars. The average shrinkage values for these different systems are plotted in Figure 4.31.

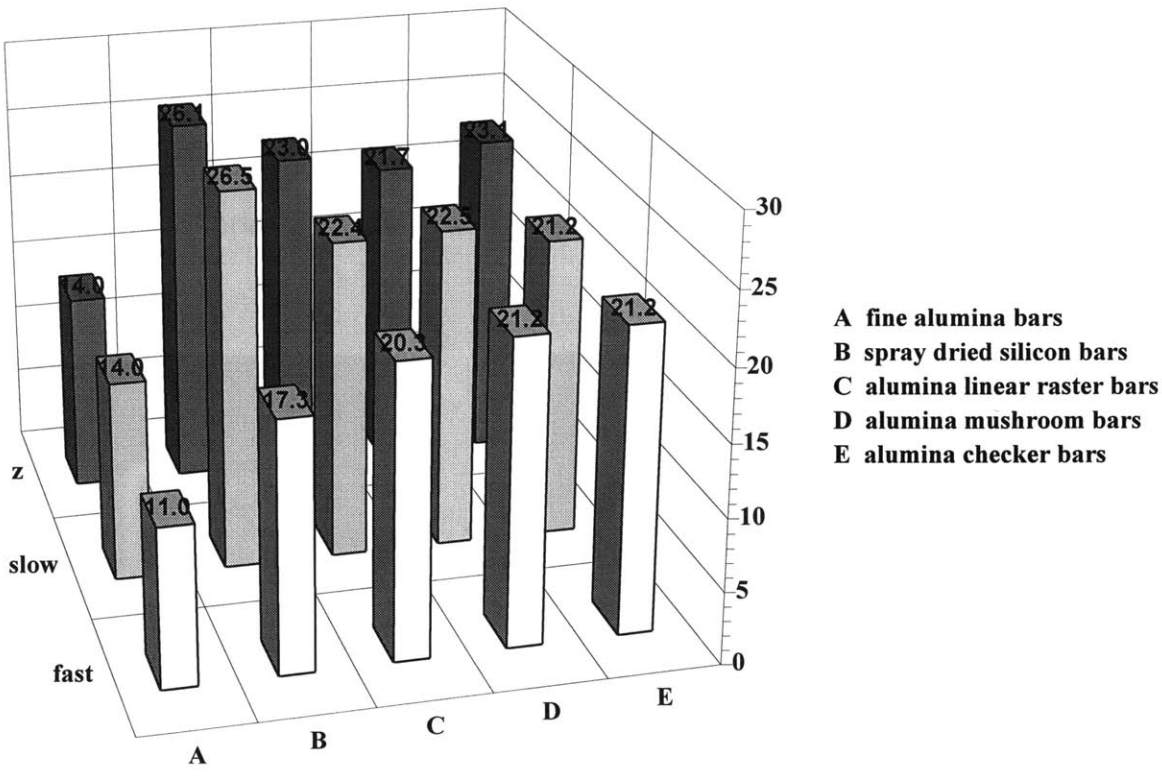

Figure 4.31 Average % shrinkage upon WIP for different powder systems and print styles along the fast, slow, and z directions.

Trends in WIP Shrinkages of Spray Dried Parts

Some of the bars warped as much as 1 mm along their entire 3.8 cm length, making it difficult to obtain accurate shrinkage measurements. However, some trends could be observed. The linear raster style generally yielded shrinkages that increased in the following order: fast axis (F) < slow axis (S) < z axis (Z). For the staggered and checker styles, the usual ordering was F < Z < S or F < Z ~ S. The reduced shrinkage in the z axis compared to the other two axes is presumably due to the closely packed line arrangement and the reduced layer height.

4.2 Alumina Prechambers

Figures 4.32 and 4.33 show three prechambers at different stages of post-processing--as-printed, just CIPed, and CIPed *and* fired. The linear shrinkage on CIP was ~20%. The net linear shrinkage in the fired part was ~35%.

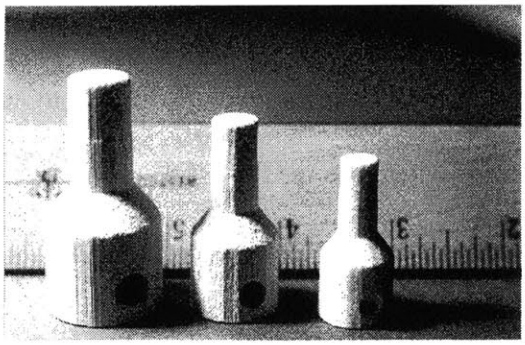

Figure 4.32 Left to right: as printed, CIPed, and CIPed & fired alumina prechambers.

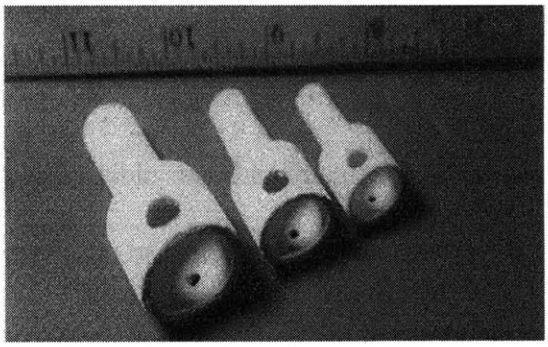

Figure 4.33 Same prechamber parts as seen from a different angle.

Several staggered fast bars were printed in the same powder bed as these complex shapes. These bars were WIPed, fired, and tested in the same way as all the other bars. The mean MOR for the 3 bars that were broken is 386 ± 11 MPa. This is higher than the mean MOR for the actual staggered fast bars (= 367 ± 23 MPa). This could be due to the fact that these bars are virtually free of contaminants while most of the other staggered fast bars contain about 30 particles/cm^2 on their tensile surface. The binder saturation in the case of the staggered bars printed along with the prechamber parts is relatively high (57.5%), very close in fact to the saturation used for the linear raster bars (61.6%). However, they do not contain long linear defects like the linear raster bars. The implication may be that excess binder deposits between granules played less of a role compared to print style-related rearrangement effects in the formation of the long intergranular pores found in linear raster bars.

4.3 Silicon Nitride Parts

The bulk density of silicon nitride bars varied between 96 and 98% of theoretical as measured by mercury porosimetry. Figure 4.34 is the fractograph of a bar with a bulk density of 96%. The elongated β-Si_3N_4 grains visible on the fracture surface are responsible for the high fracture toughness characteristic of sintered Si_3N_4 ceramics.

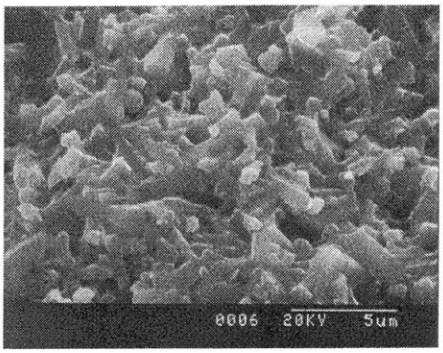

Figure 4.34 Fractograph of Si_3N_4 part showing elongated β-Si_3N_4 grains.

The MOR average for 10 Si_3N_4 bars was 570 ± 112 MPa. These represent the highest fracture strengths obtained so far for structural ceramic parts fabricated via 3DP.

CHAPTER 5

CONCLUSIONS

Four-point bend testing of green and fired bars indicated that the strength anisotropy found in as-printed green bars was largely eliminated during the subsequent Warm Isostatic Pressing (WIP) and firing steps. While the ratio of strength along the fast vs. the z axis can be as large as 3 in the case of green bars, strengths of fired bars are almost identical within each print style. Mechanical strength is virtually isotropic for 3DP-derived bars in the fired state. This result is shown in Figure 4.1, which also illustrates that WIP generally results in higher fired MORs than CIP (Cold Isostatic Pressing).

Print style, i.e. layer thickness, line spacing, binder saturation, line arrangement, and droplet placement (proportional deflection) are identified as important parameters that determine the mechanical and microstructural properties of both green and as-fired bars made out of spray dried alumina.

The simple linear raster scan yields the lowest fired strengths, suggesting that the average strength limiting flaws are larger than the average strength limiting flaws in the staggered and the checker bars. Micrographic evidence substantiates this observation. The major cause for failure in linear raster bars is found to be 3DP-induced intergranular

porosity. These defects measure up to 320 μm and are caused by granules that the isopressing step has failed to collapse completely. The differential sintering between the uncollapsed granules and the surrounding collapsed powder mass creates or exaggerates the already existing intergranular pores.

3DP-induced intergranular porosity is substantially reduced (< 100 μm) in the case of staggered and checker bars. The strength limiting flaws in those cases are found to be contaminant metal particles (~100μm in diameter). The reduced layer height and the staggered line arrangement is thought to be the cause for the reduction in the size and number of 3DP-induced intergranular pores. The highest fired alumina MORs were in the range of ~400 MPa.

Green strength is found to be the highest along the fast axis, and lowest along the z (Figure 4.14). The green strength depends on loading direction and surface characteristics. Tensile forces cutting *along* the large interlaminar defects yield lower MORs than those cutting *across* interlaminar defects. The higher number of defects found on the back and bottom surfaces of bars initiate cracks more efficiently, leading to lower green MORs than the front and the top surfaces, respectively. Proportional deflection (checker style) is found to increase the stitching along the slow axis by allowing greater overlap between adjacent lines (Figure 4.15).

Stereomicroscopic examination of single, double, and quadruple line sequences reveals important facts about the mechanisms of line and defect formation in low-cohesive strength spray dried alumina powder beds printed with Acrysol. Line merging and missing lines are identified as the main causes for defect formation. The shrinkage

that accompanies line merging and drying is thought to be responsible for the gaps that are observed between pairs of lines in optical micrographs of polished cross sections of partially sintered linear raster bars. The staggering of lines and the increased line spacing in the case of staggered bars help to avoid line merging and thus the formation of these large intergranular voids that persist through isostatic pressing and firing.

Pre-ignition chambers (prechambers) were fabricated. The current CIP step was modified to allow CIP of these complex shapes. The hollow interior had to be filled with PEG (M_w = 8000) powder prior to CIP. The PEG was dissolved away in cold water (room temperature) after CIP. The 3D-printed binder was thermally decomposed prior to firing of the parts.

Silicon nitride parts were fabricated via press-rolling of fine powders. The fired parts varied between 96 and 98% of theoretical density and had an average MOR of 570 MPa in four-point bend testing.

REFERENCES

Borland, S.W., Wu, B.M., Cima, L.G., Giordano, R.A., Sachs, E.M., and Cima, M.J., "Solid free from fabrication of reticulated structures from biomedical polymers," (submitted for publication in *Biomaterials*).

Bredt, J.F., "Binder Stability and Powder\Binder Interaction in Three Dimensional Printing," D. Ph. Thesis, Dept. Mechanical Engineering, Massachusetts Institute of Technology, Jan. 1995.

Bruch, C.A., "Sintering Kinetics for the High Density Alumina Process," *Am. Ceram. Soc. Bull.*, **41** [12] 799-806 (1962).

Burke, J.E., *J. Amer. Ceram. Soc.* **40**, 80 (1957).

Burke, J.E. and Rosolowski, J.H., Sintering; in *Treatise on Solid State Chemistry IV*, N.B. Hannay, ed., Plenum Press, New York (1974).

Carbone, T.J. and Reed, J.S., "Dependence of Sintering Response with a Constant Rate of Heating on Processing-Related Pore Distributions,"*Am. Ceram. Soc. Bull.*, **57** [8] 752-755 (1978).

Carniglia, S.C., *J. Amer. Ceram. Soc.* **55**, 243 (1972).

Charnnarong, J., Sachs, E., unpublished results, 1994.

Coble, R.L., *J. Am. Ceram. Soc.* **41**, 55 (1958).

Coble, R.L., *Kinetics of High Temperature Processes*, edited by Kingery, W.D. (Technology Press, Cambridge, Massachusetts, and John Wiley & Sons, Inc., New York, 1959).

Coble, R.L., *Ceram. Abstr.*, 1960, October, p. 246i.

Coble, R.L., *J. Appl. Phys.* **32**, I: p. 787, II: p. 793 (1961).

Coble, R.L. and Burke, J.E., *Progr. Ceram. Sci.* **3**, 197 (1963).

Cook, R.F., Lawn, B.R., Fairbanks, C.J., *J. Am. Ceram. Soc.*, **68**, 604-615.

Davidge, R.W. and Evans, A.G., *Mater. Sci. Eng.* **6**, 281 (1970).

Gasthuber, H., Heinrich, J., Huber, J., Steiner, M., Bunk, W., "HIPRBSN Prechambers for Diesel Engines," 3rd International Symposium on Ceramic Materials & Components for Engines (1988).

Gauckler, L.J. "Processing and Properties of Advanced Structural Ceramics," Ch. 5 in *High-Tech Ceramics*, edited by Gernot Kostorz (1988).

Greskovich, C., "Effect of Green Density on the Initial Sintering of Alumina," *Phys. Sintering*, **4** 33-46 (1972).

Griffin, C., Daufenbach, J., and McMillin, S., "Desktop Manufacturing: LOM vs. Pressing," **73** [8] 109-113 (1994).

Griffith, M.L., and Halloran, J.W., "Ultraviolet Curing of Highly Loaded Ceramic Suspensions for Stereolithography of Ceramics," *SFF Symp. Proc.* (1994).

Kamiya, H., Isomura K., Jimbo, G., "Powder Processing for the Fabrication of Si_3N_4 Ceramics: I, Influence of Spray-Dried Granule Strength on Pore Size Distribution in Green Compacts," *J. Am. Ceram. Soc.*, **78** [1] 49-57 (1995).

Kingery W.D. and Berg M., *J. Appl. Phys.* **26**, 1205 (1955).

Kingery, W.D., Bowen, H.K., and Uhlmann, D.R., *Introduction to Ceramics, 2nd Edition,* John Wiley & Sons, p. 488 (1976).

Lange, F.F. and Metcalf, M., "Processing-Related Fracture Origins: II, Agglomerate Motion and Cracklike Internal Surfaces Caused by Differential Sintering," *J. Amer. Ceram. Soc.*, **66** [6] 398-406 (1983).

Lauder, A., Cima, M.J., Sachs, E.M., and Fan, T., "Three-Dimensional Printing: Surface Finsh and Microstructure of Rapid Prototyped Components," *Mat. Res. Soc. Symp. Proc.* Vol. 249 (1992).

Lee, J., "Powder Layer Generation for Three Dimensional Printing," S.M. Thesis, Dept. of Mechanical Engineering, Massachusetts Institute of Technology, June 1992.

Michaels, S., Sachs, E.M., Cima, M.J., "Metal Parts Generation by Three Dimensional Printing;" *Solid Freeform Fabrication Symposium Proceed.* 244-250 (1992).

Nammour, D., "Fabrication of Glass-Ceramic Components via 3DP," S.M., 1995.

Nunomura, S., Nakayama, J., Abe, H., Kamigaito, O., "Mechanical Properties," Ch. 12 in *Advanced Technical Ceramics* edited by Somiya, S (1989).

Onoda, G.Y., "Theoretical Strength of Dried Green Bodies with Organic Binders," *J. Am. Ceram. Soc.*, **59** [5] 236-239 (1976).

Peelen, J.G.J. and Metselaar, R., *J. Appl. Phys.* **45**, 216 (1974).

Rhines, F.N., Birchenall, C.E., and Hughes, L.A., *Trans. AIME* **188**, p. 378 (1950).

Sachs, E., Curodeau, A., Gossard, D., Jee, H., Cima, M.J., Caldarise, S., "Surface Texture by 3D Printing," *SFF Symp. Proceed.* (1994).

Smith, C.S., *Trans. AIME* **175**, 15 (1948).

Subramanian, P.K., Vail, N.K., Barlow, J.W., and Marcus, H.L., "Anisotropy in Alumina Processed by SLS," *SFF Symp. Proceed.* (1994).

Yoo, J., Cima, M.J., Khanuja, J., Sachs, E.M., "Structural Ceramic Components by 3D Printing," *SFF Symposium Proceedings*, Univ. of Texas, 40-50, 1993.

Yoo, J., Cima, M.J., Sachs, E., Suresh, S., "Fabrication and Microstructural Control of Advanced Ceramic Components by 3DP," *Ceram. Eng. & Sci. Proceed.*, Cocoa Beach Conf., January, 1995.

Youshaw R.A. and Halloran J.W., "Compaction of Spray-Dried Powders," *Am. Ceram. Soc. Bull.* **61** [2] 227-230 (1982).

FIRED LINEAR RASTER BAR MORs

type of bar & WIP or CIP	max. load(N)	cham. correct. MOR (MPa)	average MOR CIP vs. WIP	stdev (MPa)
FAST				
CIP	99.56	345.14		
CIP	103.4	358.45		
CIP	83.81	290.54		
CIP	81.76	283.43		
CIP	68.17	236.32		
CIP	69.73	241.73		
CIP	73.44	254.59		
CIP	74.84	259.45		
CIP	94.5	327.60		
CIP	104.5	362.27	295.95	48.82
WIP	75.16	260.55		
WIP	88.15	305.59		
WIP	74.62	258.68		
WIP	103.7	359.49		
WIP	81.1	281.15		
WIP	89.37	309.82		
WIP	119	412.53		
WIP	107.7	373.36		
WIP	117	405.60		
WIP	97.1	336.61		
WIP	121.3	420.51	338.54	60.01
SLOW				
CIP	92.77	321.60		
CIP	92.25	319.80		
CIP	87	301.60		
CIP	102.9	356.72		
CIP	89.69	310.93		
CIP	92.1	319.28		
CIP	87.4	302.99		
CIP	84.88	294.25		
CIP	85.14	295.15		
CIP	77.24	267.77	309.01	23.24

type of bar & WIP or CIP	max. load(N)	cham. correct. MOR (MPa)	average MOR CIP vs. WIP	stdev (MPa)
SLOW				
WIP	79.44	275.39		
WIP	84.33	292.34		
WIP	88.6	307.15		
WIP	94.11	326.25		
WIP	75.33	261.14		
WIP	97.47	337.90		
WIP	104.5	362.27		
WIP	113.9	394.85		
WIP	110.1	381.68		
WIP	77.95	270.23		
WIP	93.49	324.10	321.21	45.18
Z				
CIP	77.78	269.64		
CIP	79	273.87		
CIP	92.84	321.85		
CIP	80.82	280.18		
CIP	66.22	229.56		
CIP	65.02	225.40		
CIP	81.61	282.91		
CIP	78.5	272.13		
CIP	74.15	257.05		
CIP	81.35	282.01		
CIP	81.93	284.02	270.78	26.65
WIP	90.55	313.91		
WIP	94.49	327.57		
WIP	105.4	365.39		
WIP	102.2	354.29		
WIP	104.4	361.92		
WIP	105.8	366.77		
WIP	108.5	376.13		
WIP	102.1	353.95		
WIP	87.53	303.44	347.04	25.67

FIRED STAGGERED BAR MORs

type of bar	max. load(N)	cham. correct. MOR (MPa)	average MOR (MPa)	stdev (MPa)
FAST	97.82	339.25		
	113.8	394.47		
	114.4	396.55		
	106.2	368.16		
	70.38	337.17		
	105.7	366.39		
	105.8	366.81	366.97	23.42
SLOW	115.5	400.40		
	113.7	394.16		
	110.1	381.68		
	111.7	387.19		
	119.9	415.69	395.82	13.16
Z	95.7	331.76		
	101.1	350.48		
	95.49	331.03		
	129.2	447.93		
	101.7	352.56		
	123.1	426.71		
	115.2	399.36	377.12	47.37

FIRED CHECKER BAR MORs

type of bar	max. load(N)	cham. correct. MOR (MPa)	average MOR (MPa)	stdev (MPa)
FAST	83.98	291.1		
	98.81	342.5		
	99.44	344.7		
	67.94	235.5		
	93.17	323.0		
	104.2	361.2		
	110.7	383.8		
	103.8	359.8	330.2	47.24
SLOW	97.3	337.3		
	112.7	390.7		
	113.9	394.9		
	108.5	376.1		
	111.8	387.6		
	108.7	376.8		
	111.1	385.1		
	122.3	424.0		
	103.3	358.1		
	109.3	378.9		
	101.7	352.6		
	123	426.4		
	99.49	344.9		
	113.1	392.1	380.4	26.26
Z	81.4	282.2		
	97.67	338.6		
	86.04	298.3		
	86.84	301.0		
	103.5	358.8		
	91.4	316.9		
	101.4	351.5		
	93.4	323.8		
	90.3	313.0		
	94.23	326.7	321.1	24.06
COMPLEX PART BARS	109.9	381		
	114.9	398.3		
	109.4	379.3	386.2	10.5

GREEN LINEAR RASTER BAR MORs

type of bar	tensile surface	loading direction	max. load(g)	MOR (MPa)	average MOR (fast tops, etc.)	stdev	average MOR (fast 1s, 2s, etc.)	stdev	average MOR (fasts, slows, zs)	stdev
FAST	top	1	547	0.89						
	top	1	483.1	0.78						
	top	1	444.2	0.72						
	top	1	482.3	0.78	0.79	0.07				
	bottom	1	412.7	0.67						
	bottom	1	481.7	0.78						
	bottom	1	377.2	0.61	0.69	0.09	0.75	0.09		
	back	2	541.6	0.94						
	back	2	559.6	0.97						
	back	2	510	0.89	0.93	0.04				
	front	2	545.6	0.95						
	front	2	581.8	1.01					**FAST**	
	front	2	584.9	1.02	0.99	0.04	0.96	0.05	0.85	0.13
SLOW	top	3	337.9	0.55						
	top	3	372.9	0.61						
	top	3	266.5	0.43						
	top	3	189.9	0.31						
	top	3	306	0.50	0.48	0.12				
	bottom	3	261	0.43						
	bottom	3	308.3	0.50						
	bottom	3	224.9	0.37	0.43	0.07	0.46	0.10		
	right	4	331.7	0.55						
	right	4	270.4	0.45						
	right	4	327	0.54	0.52	0.06				
	left	4	387	0.64						
	left	4	385.2	0.64						
	left	4	326.4	0.54					**SLOW**	
	left	4	305.5	0.51	0.58	0.07	0.56	0.07	0.51	0.10
Z	right	6	156.7	0.27						
	right	6	171.5	0.30						
	right	6	140.2	0.24	0.27	0.03				
	left	6	164.2	0.29						
	left	6	163	0.28						
	left	6	152.7	0.27	0.28	0.01	0.28	0.02		
	front	5	183.5	0.33						
	front	5	171.6	0.31						
	front	5	152.2	0.27	0.30	0.03				
	back	5	139.9	0.25						
	back	5	154.4	0.28					**Z**	
	back	5	151.7	0.27	0.27	0.01	0.28	0.03	0.28	0.02

GREEN STAGGERED BAR MORs

type of bar	loading direction	max load(g)	height (mm)	width (mm)	MOR (MPa)	modified MOR	average MOR (1s, 2s, etc.)	stdev	average MOR (fasts, slows, zs)	stdev
FAST	1	271	5	5	0.47	0.75				
	1	317	5	5	0.54	0.87				
	1	295	4	5	0.58	0.93				
	1	379	5	5	0.66	1.05				
	1	325	5	5	0.52	0.83	0.89	0.11		
	2	387	5	5	0.64	1.02				
	2	371	5	5	0.67	1.08				
	2	403	5	5	0.68	1.09				
	2	352	5	5	0.56	0.89				
	2	335	5	5	0.58	0.92				
	2	370	5	5	0.62	0.99	1.00	0.08	0.95	0.11
SLOW	3	125	5	5	0.19	0.31				
	3	134	5	5	0.23	0.36				
	3	129	5	5	0.21	0.34				
	3	111	5	5	0.18	0.29				
	3	112	5	5	0.18	0.29	0.32	0.03		
	4	141	5	5	0.22	0.36				
	4	128	5	5	0.20	0.32				
	4	165	5	5	0.26	0.41				
	4	174	5	5	0.26	0.42				
	4	171	5	5	0.27	0.43				
	4	136	5	5	0.21	0.33	0.38	0.05	0.35	0.05
Z	5	112	5	5	0.18	0.29				
	5	144	5	5	0.22	0.36				
	5	115	5	5	0.18	0.29				
	5	148	5	5	0.25	0.40				
	5	146	5	5	0.24	0.38	0.34	0.05		
	6	135	5	5	0.21	0.34				
	6	144	5	5	0.23	0.37				
	6	154	5	5	0.24	0.38				
	6	121	5	5	0.19	0.31				
	6	127	5	5	0.20	0.31	0.34	0.03	0.34	0.04

GREEN CHECKER BAR MORs

type of bar	loading direction	max load(g)	MOR (MPa)	modified MOR	average MOR (fast 1s, 2s, etc.)	stdev	average MOR (fasts, slows, zs)	stdev
FAST	1	413	0.57	0.59				
	1	405	0.56	0.58				
	1	337	0.46	0.48				
	1	413	0.57	0.59				
	1	395	0.54	0.56	0.56	0.05		
	2	435	0.57	0.59				
	2	355	0.47	0.49				
	2	498	0.65	0.68	0.59	0.10	0.57	0.06
SLOW	3	165	0.22	0.22				
	3	200	0.26	0.27				
	3	198.3	0.26	0.27				
	3	236.5	0.31	0.32				
	3	171	0.22	0.23	0.26	0.04		
	4	257	0.33	0.35				
	4	269	0.35	0.36				
	4	278	0.36	0.38	0.36	0.01	0.30	0.06
Z	5	157	0.18	0.19				
	5	147	0.17	0.18				
	5	139	0.16	0.17				
	5	181	0.21	0.22				
	5	161	0.19	0.20	0.19	0.02		
	6	140	0.16	0.17				
	6	170	0.19	0.20				
	6	190	0.22	0.22	0.20	0.03	0.19	0.02